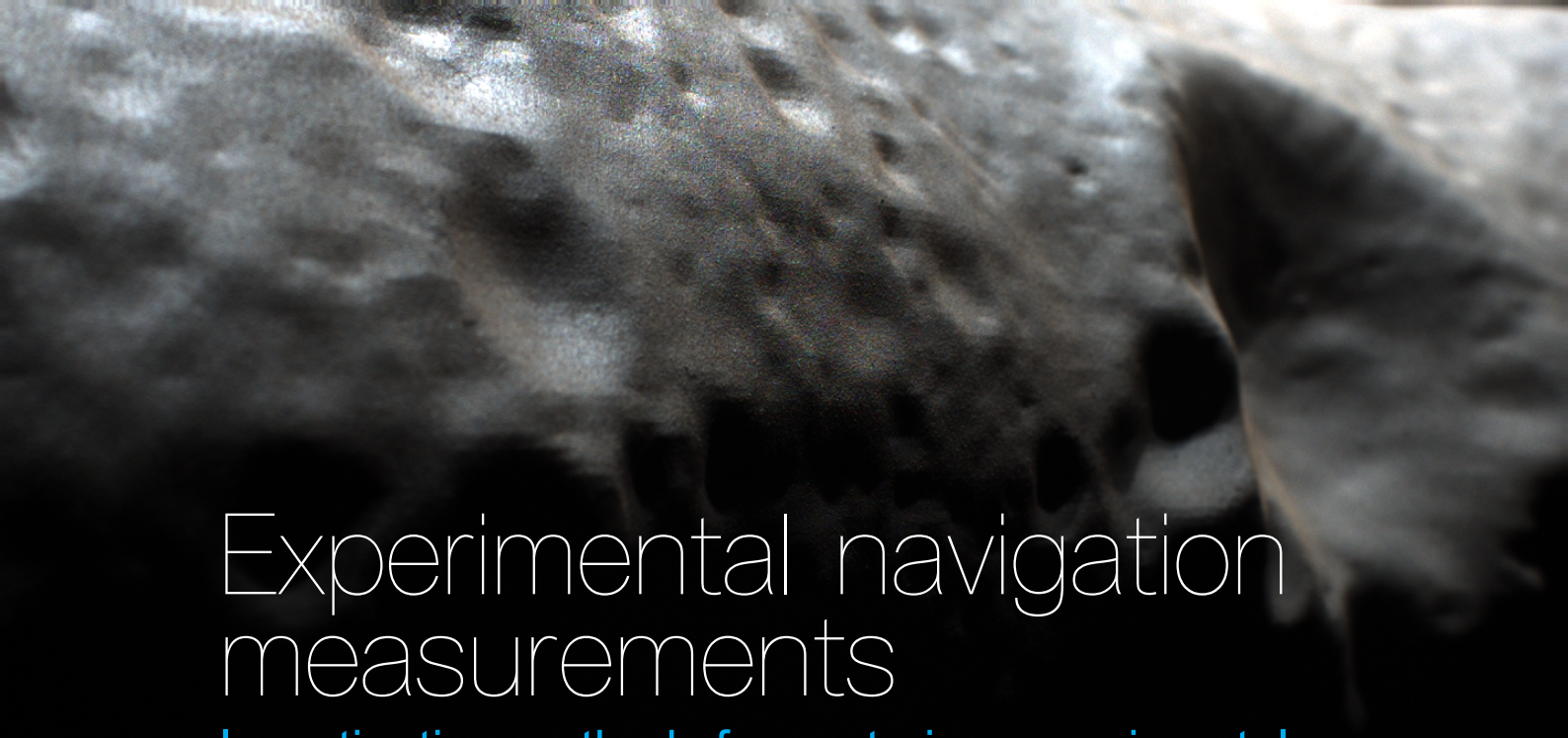

Experimental navigation measurements

Investigating methods for capturing experimental asteroid relative optical navigation images

E.N. Terwindt

Technische Universiteit Delft

TU Delft

Experimental navigation measurements

Investigating methods for capturing experimental asteroid relative optical navigation images

by

E.N. Terwindt

to obtain the degree of Master of Science
at the Delft University of Technology,
to be defended publicly on Thursday January 23, 2025 at 09:30 AM.

Student number: 4543548
Project duration: September 2023 – January 2025
Thesis committee:

Dr. J. Guo,	TU Delft, chair
Dr. P. Piron,	TU Delft, external committee member
Dr. ir. B. C. Root,	TU Delft, supervisor
Dr. ir. E. Mooij,	TU Delft, supervisor

TU Delft

Abstract

Asteroids have been a subject of interest for many years. They hold information on the early stages of the Solar System and planetary formation, they likely contain many rare minerals, and have been closely monitored to detect possible collisions with Earth. Many satellite missions to asteroid have been successfully completed over the years and more are planned for the future. However, a challenge for any asteroid mission is the irregular shape of these bodies. These irregular shapes can lead to highly irregular gravity fields that exert significant perturbations on any spacecraft that has to investigate these asteroids closely. These perturbations make navigation around asteroids challenging. So far, missions relied on human interference during orbiting phases, to correct for the perturbations experienced by the spacecraft. However, there are delays in communication that worsen with increasing distance to the spacecraft. These delays pose a threat as it could take minutes to correct any unexpected perturbations, possibly leading to a catastrophic end of the mission.

To make spacecraft more robust against these perturbations, a new autonomous navigation method was developed to include the gravity field of the asteroid in the position estimate. Several design iterations of the navigation filter have been completed before this study. A Unscented Kalman Filter has been used to estimate the spherical harmonic coefficients of the gravity fields, which was then extended to include a formation of small satellites to estimate the coefficients. A mass concentrated gravity field model was evaluated to estimate the gravity field below the Brillouin sphere, and a convolutional neural network was implemented to automate landmark tracking during navigation. These studies were all completed using numerical models, with limited error sources in the navigation measurements. There have been several studies that found benefits in the use of experimental measurements and integrated tests with flight hardware. Due to limits in numerical models, physical experiments can evaluate robustness in performance better. To further evaluate and develop the performance of the autonomous navigation, an experiment was designed to gather experimental measurements that might be used to further the development of the autonomous navigation filter.

The experiment simulated an orbit around the asteroid 433 Eros. A camera was placed in the position of the satellite to gather navigation images of a 3D printed scale model. The $10{:}1{\cdot}10^6$ scale model of the asteroid 433 Eros was created using stereolithography printing. The model was adapted to be hollow, with an internal grid structure for strength. Furthermore, as the model had to be printed in two pieces, the openings were strengthened with stringer sheets to avoid warping. It was found that a significant drying time was needed to fully dry the model before it could be cured and that the model had to be cured at room temperature to keep the dimensions as close to required as possible. The two halves were joined with alignment pins and epoxy putty, after which they were coloured using spray paint. By creating thin layers of spray paint, the surface obtained a rough surface that was more similar to the surface of 433 Eros than the bare plastic.

The 3D printed model was placed in an experimental set-up, that recreated an equatorial orbit around Eros at orbital radii of 30 km, 100 km and 200 km. A stationary camera placed at the spacecraft position at $10{:}1{\cdot}10^6$ scale, was used to capture optical navigation images of the surface of the asteroid and the asteroid was rotated to simulate an orbit with a series of image captures. The experiment was lit from above using Sun-like diodes in a dark room to further increase the realism of the experiment. A second set of numerical measurements was created using the 3D modelling software Blender, to act as a benchmark for the experimental measurements created in the test set-up. Several limitations of the experiment were found; the focal length of the camera had to be adjusted which made it an unknown, the distance measurements for the orbits were off by 1 cm, and the exact positions of the asteroid and the camera during the experiment were not recorded for later use. The first limitation could be solved by using a camera with a fixed focal length and the laboratory has since been fitted with a motion capture system which could be used for the latter two problems.

In total 5 datasets were created with 181 measurements each (one image every 2 degrees for a full rotation). The camera had a pixel size of 3.45 μm, a resolution of 1440×1080 pixels and a focal length of 8.6 mm. To evaluate the experimental dataset, the surface landmarks seen in the images were used to estimate the position of the camera. The location of the landmarks was known and

the difference in the position estimate between the experimental and numerical datasets was used to evaluate the accuracy of the dataset and thus the experiment. The position estimate was calculated by finding the intersection of the vectors between the camera and the landmarks, solving the linear system with an ordinary least squares. A bias correction was applied to adjust a misalignment in the position of the experiment camera and a sensitivity analysis was performed to find the effect of each component, namely the Cartesian position of the landmarks and the focal length of the camera, on the position estimate. It was found that the position error of the camera in the experimental dataset was in the range of 3000-4600 m for the lower orbits and up to 12000 m for the 200 km orbit radius. It was more than one order of magnitude larger than the numerical dataset, which had an error in the range of 80-450 m for the lower orbits and up to 5000 m for the 200 km orbit. The main causes to this were hypothesized to be uncertainty in the exact camera position, the landmark location with respect to the camera and the focal length. These were all direct results of the experiment set-up. Additionally, the ordinary least squares method used was not sensitive to outliers, which limited the insight into the error contribution of the individual landmarks in the position estimate.

There is still merit in using experimental images over numerical simulations. By completing an experiment, direct sensor inputs could be used in the navigation filter and hardware integration could be tested as well. By using motion capture and robotics to more accurately position all the components of the experiment, the results would become much more reliable. Even if some errors remain inherent in the experiment, it would prove robustness of the navigation filter if it functions under those conditions.

Preface

The biggest lessons I learnt during this thesis were not on the subject of space engineering but about myself. This work is the final chapter of my adventures at the TU Delft and I am very proud of the effort I put into it. It was not the easiest chapter, but that will make it all the more rewarding to look back on in the future. All this would not have been possible without the guidance of my supervisors Bart and Erwin, an incredible thank you to you both. Our meetings were a highlight every week and I do not think I would have come out so well on the other side of this without your help, and most of all your understanding.

Thank you to all my friends for putting up with me when I needed to vent, and for distracting me in the evenings with fun conversations, games, dinners and movies. My teammates for providing me with my uni-free haven where I could play away frustrations and to give me goals to works towards outside of my thesis. My family for supporting me, even when they had no clue what I was doing, and for loving me regardless of achievements.

Lastly, Luigi I'm sorry it took me so long, but I'm finally done! You have been my rock these last years and I don't know how I can ever show you how much I appreciate you sitting next to me to help me focus, cooking delicious meals for me when I'm too tired to think straight and for understanding me without me having to explain myself. I love you.

E.N. Terwindt
Delft, January 2025

Contents

List of Abbreviations

Notation	Description	Page List
CCD	charge-coupled device	6, 10
CNN	convolutional neural network	2, 36
DART	Double Asteroid Redirection Test	1
DQEKF	Dual Quaternion Extended Kalman Filter	1
DSN	Deep Space Network	2, 5, 6
EKF	extended Kalman filter	1, 2
ESA	European Space Agency	2
FDM	fused deposition modelling	12, 20
GNC	guidance, navigation and control	2
IPA	isopropyl alcohol	11, 14
LED	light-emitting diode	19, 40
LRF	laser range finder	20, 22, 25, 30
mascon	mass concentration	2
MDF	medium-density fibreboard	20
NEAR	Near Earth Asteroid Rendezvous	5, 6, 7, 17, 24
OLS	ordinary least squares	29, 36, 42
OpNav	optical navigation	2, 5, 6, 9
ORL	orbital robotics lab	2
OSIRIS-REx	Origins, Spectral Interpretation, Resource Identification, Security, Regolith Explorer	5, 6, 20
PLA	polylactic acid	20
pp	principal point	22, 24, 27, 30, 31, 33
PVA	polyvinyl acetate	15, 16
SLA	stereolithography	7, 9, 12, 39
TU Delft	Delft University of Technology	1
UKF	unscented Kalman filter	1, 2

List of Symbols

Symbol	Description	Unit
Latin Letters		
$\mathbf{A}$	matrix of linear system of equations containing unit vectors	$-$
$\mathbf{d}$	vector between points on Eros and camera	m
d	distance	m
$e_{\mathbf{p},c}$	magnitude of the error in the camera position estimate	m
e_x	magnitude of the error in the estimate in the x-coordinate	m
e_z	magnitude of the error in the estimate in the z-coordinate	m
J	matrix of ones	$-$
N	sample size	$-$

n	number of rows in a matrix	–
$\mathbf{p}$	vector of position vectors all points on 433 Eros	m
p	number of columns in a matrix	–
$\mathbf{p}_c$	camera position in inertial reference frame	m
$\mathbf{p}_{c,e}$	estimated camera position in inertial reference frame	m
$\mathbf{p}_{c,t}$	true camera position in inertial reference frame	m
$\mathbf{p}_N$	position vector point N on 433 Eros	m
R	range measurement	m
$\mathbf{r}$	residual	m
$\mathbf{r}_N$	vector from point N on image plane to focal point camera	m
s	measured distance	m
$\hat{\mathbf{u}}$	unit vector	–
V_c	circular velocity	m/s
$\mathbf{x}$	vector solution to OLS	m
x	Cartesian coordinate along the x-axis in the inertial reference frame	m
$x_{c,e}$	estimated x-coordinate of the camera position in the inertial reference frame	m
y	Cartesian coordinate along the y-axis in the inertial reference frame	m
$y_{c,e}$	estimated y-coordinate of the camera position in the inertial reference frame	m
z	Cartesian coordinate along the z-axis in the inertial reference frame	m
$z_{c,e}$	estimated z-coordinate of the camera position in the inertial reference frame	m

Greek Letters

σ	standard deviation	m
σ^2	variance	m
ω	rotational velocity	rad/s

1

Introduction

In recent years the interest in asteroids has increased[1,2,3]. Asteroids hold many answers to questions about the beginning of the Solar System and planetary formation (Lissauer & De Pater, 2013). More research is being done on how to avoid asteroid collisions with Earth with, for example the Double Asteroid Redirection Test (DART)[4]. Public and political interest in asteroids is growing due the possible mineral deposits on asteroids[2,3].

The department of Space Engineering at Delft University of Technology (TU Delft) has been working on a method for autonomous navigation that can be used around asteroids (Mooij & Root, 2024). The challenge with navigation around an asteroid is that due to its non-homogeneous shape, the gravity field is also non-homogeneous. Furthermore, the mass of an asteroid may vary greatly in a manner that cannot be directly observed from its geometry. This means that any spacecraft in orbit around such an asteroid will experience large perturbations, which will only increase with lower orbits. Since asteroids are rich in rare minerals and still hold the answers to many scientific questions about the origin of our Solar System, it would be beneficial if a spacecraft could fly low enough to take measurements, or even land on the surface to collect specimens or mine the rare minerals. There have been missions in the past (and are planned for the future) where a lander is deployed to the asteroid, but these missions were not fully autonomous. The farther the asteroid is from Earth, the harder orbiting and landing will be, due to the increase in communication intervals. If unexpected perturbations throw off the orbit, it can take minutes before ground control can intervene to correct the orbit, which could lead to a catastrophic end of the mission.

To reduce this challenge, the TU Delft has been working on a navigation algorithm that includes the gravity field of the asteroid in the position estimations. Using this method, the spacecraft itself can correct for perturbations and learn more about the gravity field in a higher orbit, before reducing its orbit where perturbations are stronger. Since these perturbations are “expected” by the navigation filter ground control will not have to correct the orbit continuously. Thus, asteroids that are further away from Earth can also be studied with less risk.

Research by Razgus (2016), Bourgeaux (2020), Spee (2022) and Van Oorschot (2022) focused on the navigation filter. Razgus (2016) started by developing a Dual Quaternion Extended Kalman Filter (DQEKF), to create a more reliable navigation filter for navigation in irregular gravity fields around asteroids. He found that the filter performed better than a conventional quaterion extended Kalman filter (EKF), albeit slower. He used a cuboid gravity model in his gravity estimation, as a polyhedron gravity field estimation was too computationally heavy. In his simulation he used landmark tracking to determine the position of the spacecraft, and he found that including the gravity field in the navigation filter increased the accuracy of the estimations.

Bourgeaux (2020) continued the research by focusing more on the onboard gravity field estimation. She used an EKF and an unscented Kalman filter (UKF) to estimate the gravity field using spherical harmonics, due to its lower computational demands. The UKF was preferred, since the EKF needs

[1] https://screenrant.com/nasa-asteroid-interest-reasons-explained/ [Cited: 13-12-2024]
[2] https://www.openpr.com/news/3781582/asteroid-mining-market-to-surge-at-23-08-cagr-projected [Cited: 13-12-2024]
[3] https://edition.cnn.com/world/astroforge-asteroid-mining-nasa-spc-scn/index.html [Cited: 13-12-2024]
[4] https://science.nasa.gov/mission/dart/ [Cited: 13-12-2024]

a Jacobian matrix, which increases in complexity as estimation parameters are added. It was noted that close to the surface of the asteroid, where the irregularities in the gravity field are more noticeable, the spherical harmonics no longer hold and a different solution must be used (such as the polyhedron model). The spherical harmonics model was implemented up to degree and order 8. This model yielded an improvement of the gravity field estimation accuracy, with an error below 10%. Although a higher degree and order could give better results, it would also increase the convergence time.

After Bourgeaux found that the spherical harmonics are not valid close to the surface of the asteroids, Spee (2022) developed a navigation filter to perform gravity field estimations in the Brillouin sphere, using a mass concentration (mascon) gravity field. He considered both an EKF and a UKF; ultimately continuing with the EKF as the performance was similar to the UKF but with quicker convergence. It was found that the mascon model was better at estimating the gravity field (comparing it to a polyhedron estimation as benchmark) than using an 8th degree and order spherical harmonics (comparing it to a 15th degree and order) at lower altitudes. The EKF was able to estimate the mascon elements for a heterogeneous asteroid, and proved that the estimation of the spacecraft position and velocity improved by using this mascon model.

Van Oorschot (2022) focused more on the actual state estimation of the satellite, by creating a filter that uses sensor fusion with a star tracker, internal measurement unit, and laser ranging. Her filter estimates both the position and attitude, where Bourgeaux and Spee only estimated the position, and assumes that no prior knowledge of the asteroid is available. The simulation is similar to Razgus' approach, though no dual quaternions are used, and the state space estimation uses a different reference frame. The results yield a state estimation error that is lower than the DSN, and the filter has a response time that is four times faster than the DSN.

Additionally, Van der Heijden (2022) studied the possibility of supplementing the sensor measurements with feature detection using a convolutional neural network CNN. Using optical navigation (OpNav), the CNN could learn in orbit during initial mission phases with limited knowledge of the gravity field before arrival at the asteroid. The CNN was able to get altitude estimates with less than 50 m error. Van der Heijden suggests to validate his results "using lab generated real images" (2022, p.5).

Munuera Vilalta (2024) sought to improve the accuracy of Bourgeaux's gravity field estimations through the use of a constellation of small satellites around an asteroid. The constellation estimates the spherical harmonics coefficients up to degree and order 15 with a UKF, using optical navigation cameras and laser ranging to determine the position of the satellites. Based on Bourgeaux her findings that spherical harmonics become to computationally complex below the Brillouin sphere, Munuera Vilalta focussed on positioning the constellation above the Brillouin sphere. The constellation of small satellites had higher accuracy estimates on the gravity field than a single satellite, using the UKF designed by Munuera Vilalta.

These studies used either no noise on the sensor measurements, or Gaussian noise. To further understand what the real capabilities of this new navigation method are, an experiment was designed to first simulate sensor measurements that could be used by this filter, and later integrate the numerical filter with experimental measurements that hold real sensor errors and to truly test the robustness of the filter. The main focus of this thesis is to obtain experimental navigation images and evaluate if these experimental images are representative of the in-orbit measurements. In the future these measurements could be used for further development of the navigation filter.

As explained by Foucher et al. (2021), using real environments allows for more comprehensive and robust testing of hardware and sensors. The European Space Agency (ESA) uses the orbital robotics lab (ORL) to simulate microgravity and to test hardware and guidance, navigation and control (GNC) systems during proximity manoeuvrers, such as rendezvous missions (Zwick et al., 2018). Similarly, Dubois-Matra et al. (2024) suggest the use real imagery of a rendezvous with the ISS to train a CNN for the further development of autonomous vision-based navigation. These studies show the importance of using real measurements to test and develop hardware and software for GNC systems.

However, how would one gather experimental data of an orbit around an asteroid that is on the other side of the Solar System? Sorsa et al. (2021) successfully used 3D printed wireframe models of asteroids, to substitute numerical models with a realistic physical model for research on tomographic microwave radar measurements. Likewise, Kaasalainen et al. (2005) were able to use a clay model of an asteroid to prove that remote sensing can be successfully simulated in a laboratory.

This study aims to create an experimental dataset of navigation images in a laboratory with a scaled test set-up, using a 3D printed asteroid model. To find if and how these images can be used for the further development of navigations systems, the following research question is investigated:

How can experimental images be captured that can potentially be used to support the development of autonomous navigation systems for asteroid relative navigation?

To answer the main research question, three sub-questions were posed to gain insight into the different aspects of creating experimental optical navigation imagery. The first sub-question aims to gather information on the processes involved in creating a physical asteroid to scale, that is accurate enough for realistic measurements.

1. How can a physical asteroid model be created, to accurately reflect the real asteroid in a scaled orbit simulation?

Next, to find the limits of an experimental set-up and how to perform such an experiment, a full experimental set-up involved in gathering experimental measurements must be developed and investigated.

2. How can an experimental set-up be created to most closely simulate in-orbit conditions?

Finally, the downsides and benefits of using an experimental dataset, over a numerical dataset are considered.

3. How do experimental measurements compare to numerically simulated images for optical navigation simulations?

The structure of the report is as follows. The thesis heritage will be discussed in Chapter 2, where relevant missions are detailed, some background information is given from the literature review and the requirements for the study are given. Following this, Chapter 3 explains the process of creating the physical model of the reference asteroid. The adaptations as well as the manufacturing method and surface treatment of the model are treated. The experiment used to gather the images is described in Chapter 4. A summary of the experiment plan and its components, and a description of the datasets is given. The quality of the datasets is evaluated in Chapter 5. First, the theory behind the evaluation metrics is elaborated upon, followed by a discussion of the errors and uncertainties. Finally, Chapter 6 aims to answer the main and sub-research questions, to end with recommendations for further research.

2

Thesis Background

There are several studies and missions that precede this research. To begin with, Section 2.1 aims to give an overview of missions that are related to this thesis. These are missions to asteroids or comets and use a similar method of navigation as that is considered for the research and some include an autonomous mission phase. Next, Section 2.2 discusses decisions made during the literature review regarding the reference asteroid, reference system and the production method of the asteroid model. Lastly, Section 2.3 gives the requirements for the study.

2.1. Relevant missions

The relevant missions for this research were investigated in a literature study. Since this study pertains to autonomous navigation around an asteroid, similar asteroid missions were considered. The NEAR (Near Earth Asteroid Rendezvous) Shoemaker, Rosetta and Dawn missions were mainly used for requirements and to study their hardware and performance. Hayabusa2 and OSIRIS-REx (Origins, Spectral Interpretation, Resource Identification, Security, Regolith Explorer) were used for a more direct comparison, since these are more recent missions and had autonomous phases in their missions.

The NEAR Shoemaker mission launched in 1996 and was the first spacecraft to land on an asteroid to gather data on its physical properties. It orbited 433 Eros at orbits of 200, 50 and 30 km altitude (Cheng, 2002) before the landing and used these orbits to map the asteroid. Navigation during this phase was done using the Deep Space Network (DSN). Any OpNav was done based on imaging taken for the science objective and done by hand at ground control (Cheng et al., 1997).

The Rosetta mission was launched in 2004 and rendezvoused with comet 67P/Churyumov-Gersimenko in 2014. The spacecraft lowered its orbit from 100 km to a mapping orbit at 20 km before delivering the lander (Muñoz et al., 2012). The approach phase depended on OpNav due to large uncertainties in the trajectory of the comet. A combination of radiometric tracking and OpNav through landmark tracking was used while Rosetta was orbiting the comet and all navigation was done on ground (Muñoz et al., 2012).

Dawn was launched in 2007 and rendezvoused with an asteroid, 4 Vesta, and a minor planet, 1 Ceres. The lowest altitude mean altitude at Vesta was less then 200 km (Russel et al., 2005), and for Ceres around 35 km (Han et al., 2019). While the Dawn probe was cruising, the DSN was used for navigation and on approach cameras were used for manual landmark tracking (Russel et al., 2005), similar to NEAR.

The Hayabusa2 mission becomes more relevant for this study since it was launched more recently (in 2014) and it has an autonomous mission phase. The spacecraft was sent to the asteroid Ryugu for a sample return mission. The first 1.5 years in orbit around Ryugu was spent mapping the asteroid, after which the orbit was lowered to 20 km for more science measurements and more accurate landmark mapping (Watanabe et al., 2017), before it landed to collect samples. During approach and in the first phase the DSN was used for navigation, together with optical navigation cameras (Tsuda et al., 2020) which were used for manual landmark tracking. In the second phase laser altimetry was added as a mapping and landmark tracking method (Watanabe et al., 2017). The final landing stage started at an altitude of 5 km at which point the vertical navigation was done autonomously, and the final 30 m of the

landing was navigated fully autonomously by using landmark tracking via the optical imaging and laser altimetry (Oshima et al., 2022).

The navigation camera of Hayabusa2 as described by Suzuki et al. (2017), has a focal length of 10.22 mm, a field of view of 69.71 degrees and a CCD (a charge-coupled device, which is the image sensor in this type of digital camera) of 1024x1024 pixels. The surface resolution at the minimal height (roughly 11.4 km in a 30 km circular equatorial orbit around Eros) is thus 13.5 m. The main navigation constraint for Hayabusa2 was that the asteroid-relative position uncertainty should not exceed 2 km and 0.1 m/s (2.5σ) at arrival, but the actual accuracy at the time of arrival was much better at less than 100 m and 0.01 m/s (Tsuda et al., 2020). The accuracies of the individual navigation measurements were around 1 m in random error and 10 m bias in position, and around 1 mm/s line-of-sight velocity for X-band DSN measurements. Hayabusa2 showed it is possible to have autonomous navigation on board a spacecraft, at least for landing in close proximity with clear landmarks. The next step would be expanding this autonomous phase to include the mapping stages of a mission and maintaining a stable orbit.

OSIRIS-REx was launched most recently, in 2016, to the asteroid Bennu. OSIRIS-REx was a sample return mission as well. Since Bennu is a smaller asteroid, the OSIRIS-REx spacecraft was able to orbit at much lower altitudes. On approach the DSN was used for navigation, in combination with star-field tracking (Lauretta et al., 2017). The first phase in orbit around Bennu was a mapping phase, completed in a circular orbit with a radius of 1.5 km. The second phase reduced the orbit to allow for more accurate mapping of the asteroid, where the altitude got as low as 225 m (Bedshore et al., 2015) before an autonomous touch-and-go landing was performed. During the proximity phases two separate methods of navigation were used. Laser altimetry was used to verify altitudes, and OpNav was used for landmark tracking (Lauretta et al., 2017). The initial plan was to perform the autonomous touch-and-go using only the laser altimetry for navigation, however that method was deemed to be unsuitable due to reliability issues (Lorenz et al., 2017). Therefore, the landmark tracking was also done autonomously during the touch-and-go, using a landmark map that was created manually earlier in the mission. Both methods were performed simultaneously and the circumstances dictated which method took precedence.

The main requirement for the navigation performance was stated in MRD-656: ”OSIRIS-REx shall predict spacecraft position in Orbital B such that predictions 24 hours after OD cutoff agree to the current (definitive) position estimates to within 20, 85, and 7 meters (goal - 6, 24, and 5 meters), all 3-sigma values, in radial, along-track, and cross track (orbit-normal) directions, respectively.” (Antreasian et al., 2022, p. 6). The orbit determination performance that was achieved during the mission was far below the requirement, and had 24 hour 1σ state errors of 0.20 m in radial, 3.2 m in transverse and 0.22 m normal directions, as discussed by Antreasian et al. (2022), and similarly found previously by Berry et al. (2015) who determined a possible 3σ navigation uncertainty of 0.529 m, 3.132 m and 0.633 m in radial, in-track and cross-track directions, and 0.173 mm/s, 0.035 mm/s and 0.077 mm/s. The OSIRIS-REx mission had a significantly higher accuracy for its navigation performance than the Hayabusa2 mission (in the order of 10^{-1} m instead of 10^{2} m (Antreasian et al., 2022; Tsuda et al., 2020)), however it also had a much smaller target and lower altitudes which made this possible. The lesson OSIRIS-REx teaches is that a combination of sensors should be used for autonomous navigation and that again the combination of laser altimetry with OpNav makes this possible.

2.2. Relevant background

Several decisions on the thesis research were made during the literature phase; the reference asteroid that was used in the experiment, the type of orbit that was simulated, the reference system in which the position of the simulated spacecraft was expressed, the method of creating the physical model of the reference asteroid and the requirements.

2.2.1. Reference asteroid

The reference asteroid that was used in this thesis was chosen to be asteroid 433 Eros, for several reasons. Firstly, since the NEAR mission previously orbited 433 Eros (or simply Eros), there is a lot of information available on this asteroid already. Secondly, to answer sub- question 1, a 3D model of the reference asteroid is required. Gaskell (2004) has previously created such a model with the imagery from NEAR. Thirdly, of the previous theses discussed in Chapter 1, Bourgeaux (2020) and Spee (2022)

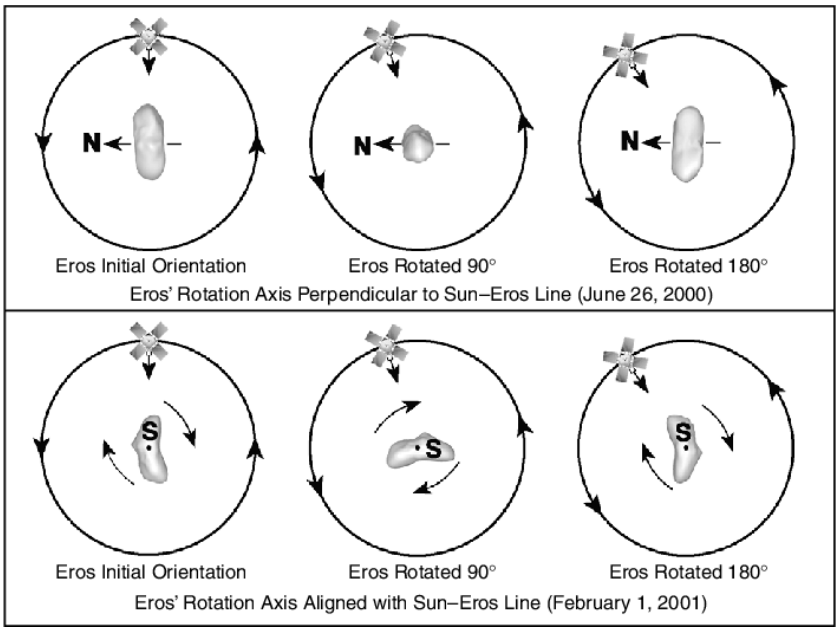

Figure 2.1: "NEAR Shoemaker's orbital geometry at Eros in June 2000 and February 2001 (view from Sun; orbit size: 50 × 50 km)" (from Farquhar et al., 2002)

and Munuera Vilalta (2024) used Eros in their analyses due to its very irregular shape and its highly irregular gravity field, which makes it a good candidate to test autonomous navigation. The extent of Eros is 34.4 x 11.2 x 11.2 km, with an effective diameter of 16.84 km and it has a rotational period of 5.27 hours[1]. To continue with the cases studied in the previous theses, the simulated orbit around Eros will be an equatorial orbit. Figure 2.1 shows how NEAR orbited around Eros. Around NEAR's arrival, Eros its rotation axis was aligned with the Sun-Eros line (visible in the bottom half of the image), which is the orbit that will be simulated, since this allows the lighting simulation in the experiment to be simplified to a static scenario.

2.2.2. Reference system

The reference frame used to express the position of the spacecraft with respect to Eros is a quasi-inertial reference frame. This frame is fixed in space and does not rotate along with Eros. Figure 2.2 shows the reference frame in black. The red reference frame is the asteroid reference frame which is fixed to a point on Eros, and rotates along at the same rotational rate of $\omega = 3.312 \cdot 10^{-4}$ rad/s as Eros[1]. The x-axis is fixed to the intersection of the prime meridian and the equator of Eros, the z-axis is located perpendicular to the x-axis through the spin pole (Thomas et al., 2000) and the y-axis completes the right handed coordinate system. In the simulation the z-axis is be Eros' rotation axis.

During the later analysis in Chapter 5, the points identified on the surface of Eros are expressed in the quasi-inertial reference frame, because the camera used in the experiment (as discussed in Chapter 4), is set-up along the y-axis of the quasi-inertial reference frame.

2.2.3. Production method asteroid model

During the literature review it was decided that the asteroid model would be created using the 3D model made by Gaskell (2008). Since Sorsa et al. (2021) had success using a 3D printed asteroid model in their research, prototyping using a 3D printer has relatively low cost and a Formlabs Form 3L[2] was readily available, it was decided to use 3D printing. The Formlabs Form 3L is a stereolithography (SLA) printer, more commonly known as a resin printer. Based on the resolution of navigation cameras used in the heritage missions, the required scale of the model could be determined, using the layer height as the limiting factor. The printer and the process of creating the asteroid model are discussed in detail in Chapter 3.

[1] https://ssd.jpl.nasa.gov/tools/sbdb_lookup.html#/?sstr=433%20Eros&view=OPA [Cited: 06-06-2023]
[2] https://formlabs.com/3d-printers/form-3l/ [Cited: 21-06-2024]

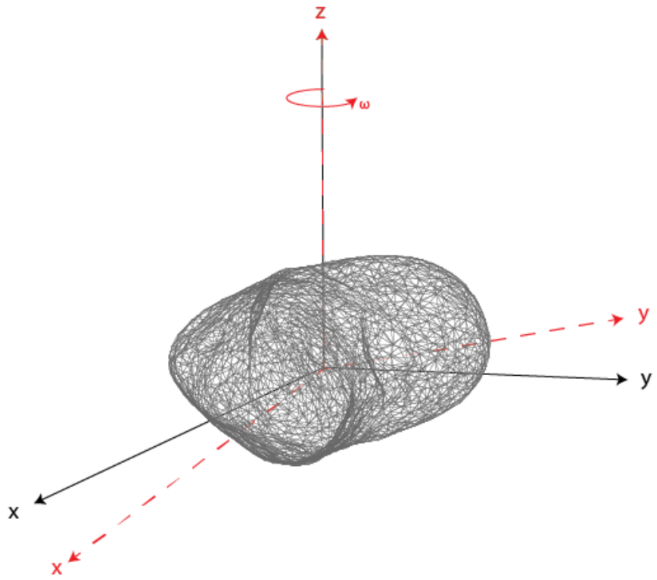

Figure 2.2: Inertial (black) and asteroid (red) reference frames, from Van Oorschot (2022)

2.3. Requirements

The requirements for the development of the experimental navigation images are stated below. Due to re-scoping of the research, several requirements were no longer relevant and are not included in the list. The system that the requirements refer to, is the experiment that is designed.

MIS-01	The mission shall consist of a single satellite in an equatorial orbit around an asteroid.
MIS-02	The mission shall use surface-based relative optical navigation.
SYS-04	The system shall be based on a mission around 433 Eros.
SYS-04.2	The system shall simulate orbits with radii of 30 km and 200 km around 433 Eros.
SYS-05	The system shall be independent of 433 Eros parameters.
SYS-06	The system shall obtain sensor measurements using a scaled asteroid model in a physical experimental test set-up.
SYS-06.2	The scale model shall be a 3D printed model of asteroid 433 Eros.
SYS-06.2.1	The scale model shall have a smaller scaled surface resolution than the resolution of the Hayabusa2 ONC-W1 at an orbital radius of 30 km.
SYS-06.2.2	The manufacturing method shall have a resolution equal to or better than the surface resolution of the shape model of 433 Eros.
SYS-06.2.3	The scale model shall have a surface roughness equal to the scaled surface roughness of 433 Eros.
SYS-06.3	The experimental navigation images shall be captured with an optical camera.
SYS-06.3.1	The experiment camera shall have a surface resolution equal to or better than the Hayabusa2 ONC-W1 navigation camera.
SYS-07	The scaled measurement error shall be less than the Hayabusa2 navigation error of 100 m.
SYS-07.1	The experiment camera distance to the scale model shall have an error of $\leq$ 1 mm.
SYS-07.2	The error in the rotational position of the simulated spacecraft shall be $\leq 1 \cdot 10^{-3}$ rad.

3

Asteroid Model

The experiment introduced in Chapter 1 needs a physical asteroid model before experimental images can be created. This model was manufactured through 3D printing with the Formlabs 3L SLA printer, as mentioned in Section 2.2. This chapter details the process involved in creating the physical model, by first discussing which model was used in Section 3.1. Next, Section 3.2 explains the steps to 3D printing, followed by Section 3.3 which discusses the surface treatment of the physical model.

3.1. 3D model Eros

The asteroid model is the basis of the experiment. As discussed in Section 2.2, 433 Eros is used as the reference asteroid. Gaskell (2004) used the imagery from the NEAR mission to create a 3D model through stereophotoclinometry. The basic steps to creating the 3D model for the experiment, which will be explained in more detail throughout the chapter, are:

1. Select 3D shape model of target asteroid
2. Determine scale for the experiment based on model and printer resolution
3. Adapt 3D model for printing
    a Create inner structure to reduce material and maintain strength
    b Add mounting system for the experiment set-up
    c Add walls against warping
    d Add alignment pins for combining model halves
4. Print model, minding orientation and print supports for quality
5. Clean, dry and cure print
6. Adhere halves together with epoxy putty
7. Add surface finish by building thin layers of spray paint to the desired surface roughness

3.1.1. Resolution

The 3D model has an average resolution of approximately 27 m/pixel and is build up out of 1.57 million vertices (Gaskell, 2008). In his original study, Gaskell used the model to predict the gravity harmonics of Eros and found that this model was more accurate compared to observed harmonics, than a laser altimetry model that was created during the mission. Since a future goal could be to apply the experiment described in Chapter 4 to autonomous navigation which includes the gravity field estimation in its time update, this model being more accurate than the laser altimetry measurements makes it more representative.

The surface resolution of the optical navigation for Hayabusa2 set the limit for the minimum required resolution of the 3D model. If the resolution of the OpNav is an order of magnitude higher than the resolution of the 3D model used for Eros, then the landmarks that might be used for landmark tracking might not be visible in the 3D model. Dombard et al. (2010) and Michikami and Hagermann (2021) performed studies on the landmarks on the surface of Eros. Both studies found that most boulders on the surface of Eros were smaller than 30 m in diameter. However, Michikami and Hagermann found that around 750 of those had a diameter of more than 30 m. Dombard et al. also looked at so called

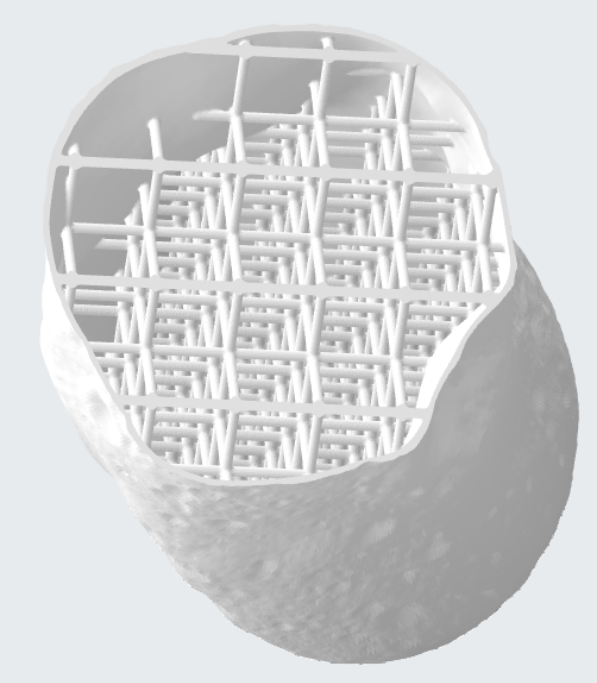

Figure 3.1: Internal structure added for strength to the asteroid model

“ponds” on the surface of Eros. These are flat low laying areas, reminiscent of ponds. They identified 334 ponds on the surface, the majority of which had a diameter greater than 30 m and ranged up to more than 200 m. Additionally, both studies noted that these landmarks are concentrated along the rotational equator. Therefore, it is assumed that the Gaskell model has landmarks visible that could be used for landmark tracking. Especially since the orbit is simulated in the experiment is equatorial.

The minimum scale for the model can be determined by scaling the resolution of the Gaskell model. Making the model too small will make the landmarks too small to print, whereas a large scale might make the model difficult to manufacture and too heavy to handle in the experiment. Following this, it was decided to use the scale $10{:}1{\cdot}10^6$ for the model, where each cm on the model is a km on Eros. The resolution of the model becomes 0.27 mm/pixel, which will be printable as will be discussed further in Subsection 3.2.1.

As previously stated in Section 2.1, the navigation camera of Hayabusa2, has a focal length of 10.22 mm, a field of view of 69.71 degrees and a CCD of 1024x1024 pixels. This leads to a minium surface resolution of 13.5 m. At $10{:}1{\cdot}10^6$ scale the representative surface resolution would be 0.14 mm. This is in the same order of magnitude as the 3D model. Thus, the Gaskell model was deemed appropriate for the experiment.

3.1.2. Adaptations

As mentioned in Section 2.2, the physical model of Eros will be created using a 3D printer. The 3D shape model as made by Gaskell is solid, so several changes had to be made to the model to make it appropriate for printing. Firstly, the model was made hollow, as the resin that will be used for printing is an expensive resource (more on that in Subsection 3.2.1). Additionally, a solid model would be very heavy and thus hard to handle and mount in a test set-up. The software that was used for adapting the model was Meshmixer. Meshmixer allows existing ”meshes” to be adjusted for 3D printing. For the final model a skin thickness of 2.5 mm was found to be sufficiently strong to avoid breaking the skin when handling the model.

Secondly, an internal structure was added to the hollow shell of the asteroid, as it is vulnerable to breaking and warping. Warping could occur during post processing of the print and any deformations in the shape would cause the asteroid surface to be less accurate for the experiment. An internal structure, see Figure 3.1, was added for strength and rigidity to circumvent this. A grid of 5 mm thick bars at 3 cm spacing was created and set at a 45 degree rotation to allow for easy printing.

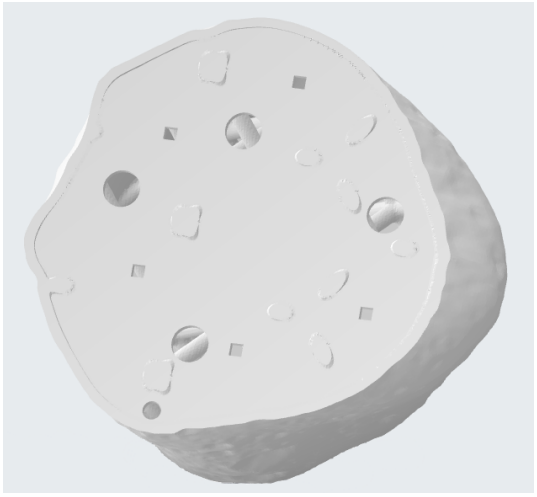

(a) Stringer sheet at the opening of the left half. The square pockets for the pins and round access holes can be observed on the surface of the stringer sheet. The larger holes are for the IPA wash and the smaller hole at the bottom is added to avoid cupping due to a vacuum when printing. The protrusions are the ends of the infill structure that are attached to the stringer sheet.

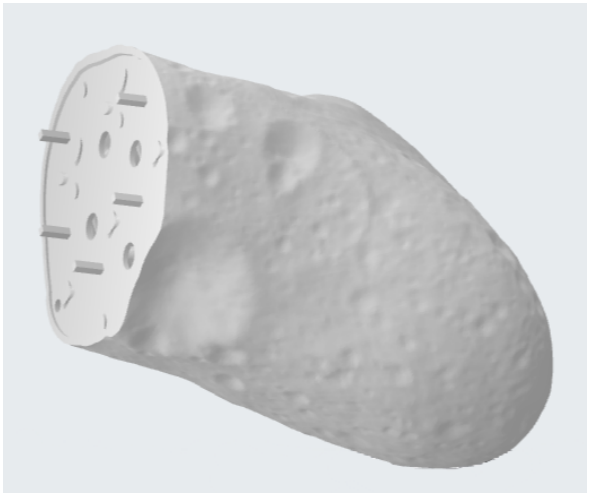

(b) Right half of the model. The same stringer sheet and access holes are added to the opening, but pins are visible. These pins will help aligning the halves when inserted into the pockets on the left side.

Figure 3.2: The left and right halves of the third iteration of the Eros scale model. Stringer sheets are visible and the pins and pockets used for alignment.

Thirdly, the asteroid shape model was divided into two halves, which has several benefits. The separate part fits in the 3D printer more easily. Also, post-processing (see Section 3.2); washing the model after printing with isopropyl alcohol (IPA), removing supports and curing the model, is more effective since it is easier to clean the internals of the print. Furthermore, the surface quality of the finished print is much better, as the print can be oriented in a way that limits the number of print supports attached to the surface. The surface of the asteroid holds all the relevant information for landmark tracking and should therefore be kept as clear by limiting printing artifacts from print support attachments.

Next, a hole was added at the south pole of the asteroid to allow a threaded insert to be placed, to enable mounting the model in the experimental set-up (see Chapter 4). A 0.25 inch threaded insert was added, which needed a 8.75 mm hole. Since resin printers create thermoset plastics, the insert had to be glued instead of melted in place.

To support the open ends of the two halves, stringer sheets are added to the opening and half way in the model (4 in total). These stringer sheets were 2 mm thick plates with 3x3x1 mm L stringers attached to the surface, spaced at 2 cm. These stringers were used to avoid warping or torquing the model after it is printed and before the resin is fully cured.

Lastly, to align the halves when they are glued together, pins and pockets (see Figure 3.2) were added to the stringer sheets at the openings. The pins were 3x3x11 mm cuboids and the pockets were 3.4x3.4 mm square hole to allow the pins to fit through. There were 5 pins added around the perimeter to ensure a secure fit. Extra holes were added to these stringer sheet to allow access to the inside of the model. The pockets and access holes can be seen in Figure 3.2a. The stringers are set on the inside of the sheet so they do not interfere when putting the two halves together.

Table 3.1 shows the final dimensions of the 3D model that was used in the experiment. Appendix A, Section A.2 contains an overview of all the prototypes that were modelled and printed during the development and testing of the manufacturing process.

3.2. Printing

3D printing is very versatile in the geometries it can print, the turnaround time for the creating, printing and testing of prototypes is short, and the facilities were available in house at the university. This section will give an overview of the considerations for printing and the lessons learned during the process. Appendix A contains a full description of all the steps needed to print a model and additional advice.

Table 3.1: All dimensions of the final 3D model of Eros.

Scale	$10{:}1{\cdot}10^6$
Skin thickness	2.5 mm
Grid infill	5 mm bars x 3 cm spacing
Stringer sheets	2 per half
Stringer sheet thickness	2 mm
L stringer dimensions	3 x 3 x 1 mm, 2 cm spacing
Washing holes	20 mm, 4 in each sheet
Cupping prevention holes	5 mm, 1 in each sheet
Mounting hole	8.75 mm inner diameter, 3.3 mm wall
Alignment pins	3 x 3 x 11 mm, 5 pins
Alignment pockets	3.4 x 3.4 mm, 5 pockets

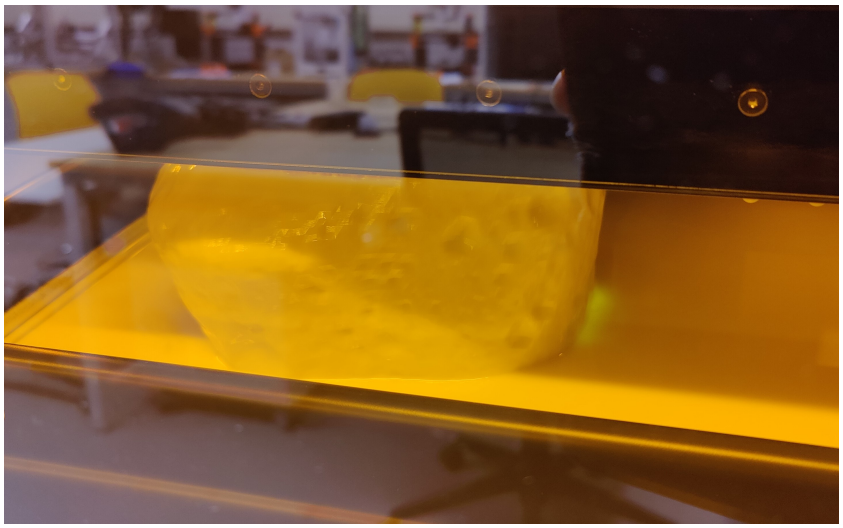

Figure 3.3: The green UV laser is visibly curing a thin layer of resin to the model as it slowly rises layer by layer out of the resin tank.

3.2.1. Printer

As mentioned in Chapter 2, the printer used was the Formlabs Form 3L[1]. The (SLA) printer, or resin printer, uses liquid resins that are slowly built up by curing thin layers with a UV laser, similar to a stalactite. In Figure 3.3 the UV light of the laser curing a layer in the printer can be seen. The advantage of a resin printer over a fused deposition modelling (FDM) printer (the more conventional 3D printer) is that SLA can print at a higher resolution since the layers can be made much more thin. The resolution for this printer, in combination with their White V4 resin, is a 0.05 mm layer thickness. The resolution of the printer is better than the surface resolution of 0.14 mentioned in Subsection 3.1.1, and thus the print layers will not create artefacts visible in the imagery. If the 3D model has a high enough definition in the surface geometry, the 3D print will not be the limiting factor in terms of resolution and realism.

3.2.2. Printing

To prepare the model for printing, Formlab's own software PreForm[2] was used. This software slices the model into the individual layers and checks whether there are any geometries which cannot be printed by the printer. Additionally, support material can be added to allow the printing of overhangs. During the prototyping phase several observations were made on the effect that the print orientation and supports have of the quality.

[1] https://formlabs.com/3d-printers/form-3l/ [Cited: 21-06-2024]
[2] https://formlabs.com/software/preform/ [Cited 21-06-2024]

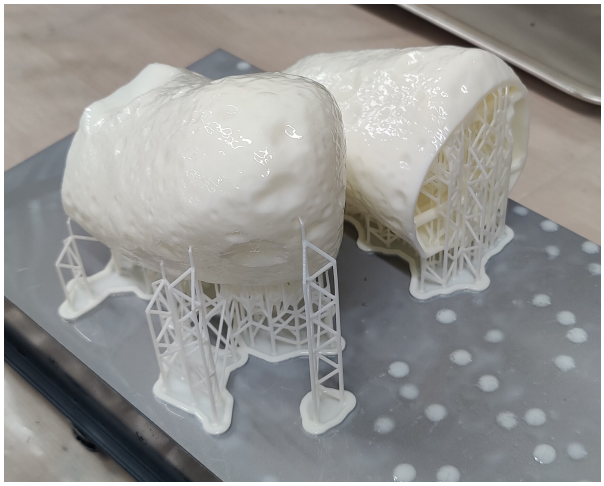

Figure 3.4: A prototype of Eros after printing, still attached to the print plate. The print supports and rafts on the print plate can be seen under the models.

Orientation The first observation that was made on the orientation, is the effect on the final geometry. If a perfectly flat face is needed, that face should not be set to be level to the print plate. The face will be printed on print supports, and it is not possible to print one large layer perfectly level into the ”air”. Therefore, the first face will be built on the print supports in small islands, and then those will become one large sheet as their area is slowly increased over the layers. Adding more supports will limit this effect, although with an increased number of supports there will also be more artifacts of the supports themselves. Which means the face will not be flat regardless. To avoid this the print can be rotated to have the face in question at an angle of >30 degrees. Using this method, supports can be avoided and the face can be printed layer by layer to be perfectly flat.

The print can be placed directly onto the print plate and thus avoiding any supports at all. However, Formlabs warns against this in the Preform software since the first layers have a different curing time to ensure proper adhesion to the print plate. This increased exposure of the UV changes the properties of the finished plastic and reduces the resolution.

Additionally, another point to take into account with the print orientation is printing sharp edges. The same holds for an edge (considering the corner of the edge pointing to the print plate) as for printing a flat face. A long thin edge cannot be printed into the air, and thus the edge will not be perfectly straight and sharp. If a sharp edge is desired, the print should be rotated to have the edges supported with the rest of the model. Thus, the edges should be printed later, so they are easy to adhere to the already printed parts of the model.

Supports and rafts As mentioned previously, adding print supports leaves artifacts. Therefore, if there is an exact geometry with small allowances, the model should be oriented to minimise the print supports attached to that geometry. The artifacts can be removed after the print is completed, but this is done by using small knives and sandpaper which influence the final geometry and allowances.

The print supports are in turn attached to rafts. Rafts are the surfaces printed directly onto the print plate, onto which the print supports are built and can be seen in Figure 3.4. There are two options for the raft size. Either a full raft can be used, where most of the supports are attached to a single or several large rafts; or mini rafts can be used, where almost every support is attached to its own small raft. A benefit of a full raft is that the model does not need to be removed from the raft until al post-processing is complete. Mini rafts are more easy to remove from the print plate. However, a large model might be too heavy for the smaller rafts, causing the print to come loose from the print plate.

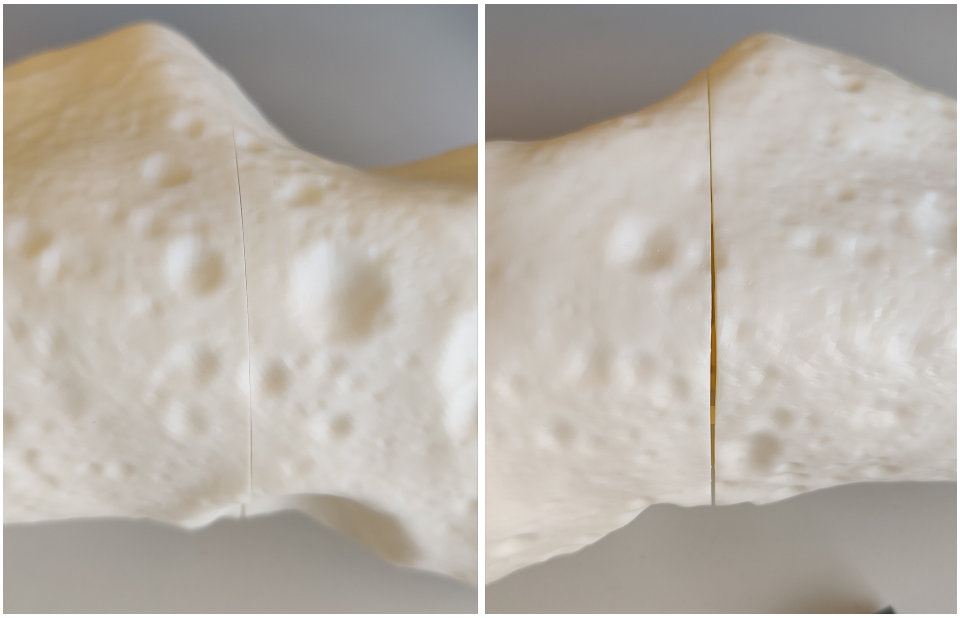

Figure 3.5: Failed print of an Eros scale model at $7{,}5{:}1{\cdot}10^6$ scale, fourth iteration. A warp was noticed after post-processing at the bottom edge of the seam between the two halves.

3.2.3. Washing and drying

After the model is printed, it has to be washed in an IPA bath to remove the uncured resin that is still stuck to the outside of the print. For this, the Form Wash L[3] was used. The model is submerged in IPA and the bath agitates the IPA so it flows along the surface and clears off the resin by dissolving it.

Initially, as per instruction (Formlabs, 2021), the model was washed and left to dry until the surface was no longer damp. After this, the model was cured in a UV curing station (more on this in Subsection 3.2.4). However, it was observed that the prototypes warped during post-processing, which caused the two halves to no longer fit together neatly, as can be seen in Figure 3.5. User feedback suggested that warping could be caused by not letting the model dry for long enough[4], as the cured resin can absorb some IPA and if that has not completely dried it can outgas while it is curing in the curer. This was considered a possible cause of the warping. Therefore, the print was allowed to dry under a vacuum hood for at least 2 days to ensure no IPA was caught in the plastic. This hypothesis was supported by the location of the warping. The warp depicted in Figure 3.5 occurred at the lowest point of the model as it was set to dry. The model dried fastest at the highest points, as the IPA flowed down. If this model was in fact cured too fast, it seems logical that the section that would be last to dry was the section that warped most.

3.2.4. Curing

After the model has been washed and dried completely, the model needs to be cured to increase the strength of the material[5]. The manufacturer has a suggested cure cycle, in which the model is put through a preheat cycle to slowly get it to temperature and then cure it at 60 °C for 30 minutes[6]. Curing it at an elevated temperature allows the polymers to settle faster which increases the strength of the material. It was attempted to decrease this warping by increasing the length of the preheat cycle threefold, to reduce the thermal shock. This did not negate the warping. However, several users have reported that their models warped while curing with a heating cycle[7]. Therefore, the preheat and regular heat cycles were disabled to avoid warping. Since elevated temperature allows the model to reach full strength faster, the UV curing time was increased to 90 minutes to get closer to full strength

[3] https://formlabs.com/store/post-processing/form-wash-l/ [Cited 21-06-2024]
[4] https://forum.formlabs.com/t/excessive-part-warpage-during-curing/35670/5 [Cited: 21-06-2024]
[5] https://formlabs-media.formlabs.com/filer_public/ac/89/ac8963db-f54a-4cac-8fe9-fb740a7b06f1/formlabs-materials-library.pdf [Cited: 25-06-2024]
[6] https://support.formlabs.com/s/article/Form-Cure-Time-and-Temperature-Settings?language=en_US [Cited: 25-06-2024]
[7] https://forum.formlabs.com/t/excessive-part-warpage-during-curing/35670/6 [Cited: 25-06-2024]

Figure 3.6: Eros10_3 after the first coat of paint, with the halves adhered together using milliput epoxy putty. The epoxy is also used to fill the gap left by the warp of the model during post-processing and to glue in the threaded insert shown.

than it would be if it was cured for only 30 minutes without heat. This reduced the warp, but a gap between the halves maintained. An epoxy putty called milliput[8] was used to fill the gap that was left after adjusting the post-processing methods. Figure 3.6 shows the white epoxy line between the two halves of the model. This acts both as a strong adhesion to combine both halves, and as a filler to close the larger gaps.

The last gap that was left was possibly caused by to the orientation of the model in the printer. As discussed in Subsection 3.2.2, the sharp edge of the joint was the first layer to be printed. Some of the warping may be due to the lack of definition in the edge due to the limits of the printer. The orientation was selected to limit the number of supports on the surface of the model, since the surface holds all the information that is needed in the experiment. If all the print supports were located on the surface, the consequent clean up of the surface might affect the geometry that is needed by the simulated navigation camera that will be discussed in detail in Chapter 4. The future design of the model, or a different medium or method of manufacturing could be considered to minimise this problem, such as computed axial lithography[9]. While this method of 3D printing is still under development, it is a method of creating a print while it is suspended in resin. It is cured in one piece, without supports, by projecting an image of the model into highly viscus resin while rotating the resin, to obtain a three-dimensionally cured object.

3.3. Surface treatment

The asteroid comes out of the printing process as a smooth and shiny white object. Since the goal is to make the test set-up as near to life as possible, the surface of the asteroid should treated to approach what Eros looks like. Therefore, the model needs a surface finish that scatters light similarly and has a similar colour and finish.

3.3.1. Sand and glue

The first option to create a more realistic surface finish was sand. It was attempted to scatter a thin layer of sand on the surface. Two methods of application were tested. Firstly, a spray adhesive was used. Glue was sprayed on a test model of the asteroid and the sand was scattered on top of the glue and then pressed in place. However, the glue was very viscous and did not spray evenly, and was a pressure adhesive. It was hard to apply pressure evenly over the entire surface due to the irregular shape of Eros and thus it was challenging to get an even coat of the sand.

Secondly, a mixture of water and PVA (polyvinyl acetate) glue was tested, a method used in miniature model building. The first attempt was with a mixture of 1:2 PVA to water, however the viscosity of this mixture was too high, causing it to spray in a singular stream, instead of the desired mist of

[8]https://www.milliput.com/white.html [Cited: 12-11-2024]
[9]https://www.ocf.berkeley.edu/~hayden/computed-axial-lithography.php [Cited: 13-12-2024]

glue. The initial mixture was diluted to 1:5 PVA to water, which allowed droplets to form more easily. However, at this stage the droplets were still so large that clumps of sand to formed on these drops of glue, which did not allow for the even distribution of sand which was desired. To further reduce the surface tension, a single drop of dish soap was added. This resulted in an even droplet distribution of the glue and the droplet size was reduced such that the sand no longer created clumps.

The third version of the PVA-mixture was tested on a clean test model of Eros, which successfully resulted in an even distribution of sand and proper adhesion. Adding a coat of paint over the sand further improved adhesion, as the sand would not rub off when handled.

However, the sand - even though the sand grains were very fine - created shadows on the surface and the texture was too rough for the scale of the model. The sand would reduce the realism of the set-up and was therefore disregarded.

3.3.2. Paint

Instead of using the sand, the paint itself was considered for creating a rough surface finish. The model of Eros would have to be painted from the white colour of the 3D printing resin, to a colour that would resemble the true Eros more closely, which can be seen in Figure 3.7. This spray paint is applied in thin layers of microscopic droplets. Instead of applying one solid opaque layer, many thin layers were applied. This allowed the individual paint drops to dry before more were added to eventually get to an opaque layer. This creates a texture through the build-up of layers of these individually dried droplets.

The first attempts were made with a standard spray lacquer, however this paint had a glossy finish. Even with the added texture, the surface was still too reflective for a realistic surface finish on the Eros model. A second attempt was made with an extra matte paint[10], which created an effect much closer to the more dusty surface of Eros. Two colours were used to approximate the reddish gray colour of Eros. A grey base, then a layer of a reddish orange, another coat of grey, and finally a very fine layer of the orange to attempt to recreate the hue of the sand on Eros. On the final model that was used in the experiment both halves were first sprayed separately with the first two layers, after which the halves were glued together using the milliput epoxy putty mentioned in Subsection 3.2.4, and finally the last two coats of paint were added to ensure the colour is continuous over the whole model.

The final result still maintained a higher sheen to the surface than desired. It could be attempted to increase the layers of paint for a more matte finish. Furthermore, an adaptation to the model could be tested, where the surface already has an added texture that is printed on in the 3D printing process.

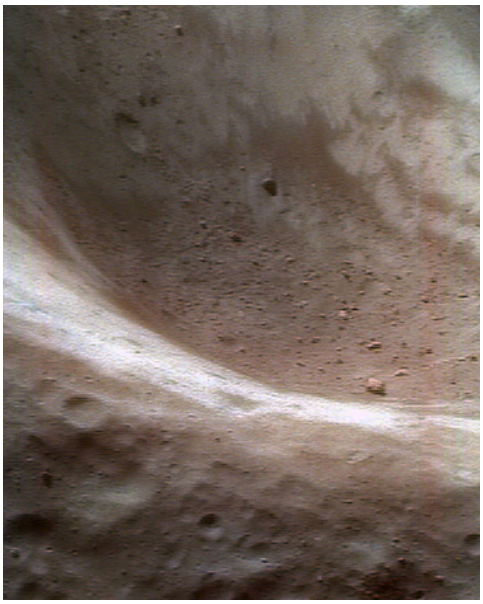

Figure 3.7: Real image of the surface of Eros captured by NEAR[11]. The appearance of the surface was used as a reference for the surface treatment

[10] MTN 94 paint in colours Pearl Grey and Dalai Orange
[11] https://nssdc.gsfc.nasa.gov/planetary/mission/near/near_eros_4.html [Cited: 11/12/2024]

4

Experiment

This chapter details all the components used and steps to the experiment. Section 4.1 gives an initial overview of all the components and summarises the experiment plan. Following this, Section 4.2 goes into more detail on the light source and Section 4.3 elaborates on how the rotation of the asteroid model was controlled. Next, Section 4.4 details which camera was used to simulate a spacecraft navigation camera and how it was calibrated. Finally, Section 4.5 discusses the datasets created during the experiment and any challenges that occurred while gathering the measurements.

4.1. Experiment plan

It was decided to use an equatorial orbit for the experiment, which means that the test set-up can be simplified to a stationary sensor suite, imaging a rotating asteroid. For part of its orbit around the Sun, an equatorial orbit orbit around Eros is perpendicular to the Eros - Sun axis, as explained in Section 2.2. This means that the set-up can be lit from the top if the sensors are ”horizontal” to the asteroid. This further simplifies the set-up, since the lighting does not have to rotate along the equator, and the simulated satellite doesn't pass between the Sun and Eros.

The orbits that will be considered in the experiment are all circular. A 30 km orbit will be used, since that is around the limit of a stable circular orbit around Eros, while experiencing significant perturbations (Chanut et al., 2014). A 200 km orbit will simulate a mapping orbit around Eros, was the case for NEAR (Cheng, 2002). A 100 km orbit was added later, as will be explained in Section 4.5.

The model of Eros is mounted in the centre of the set-up on a rotating base. The camera that is used to simulate the optical navigation measurements is mounted on a mic stand a set distance away, depending on the desired orbit. A lamp that simulates the visual spectrum from the Sun is hung from ceiling, and the entire set-up is placed in a dark room to limit the light pollution.

Figure 4.1 shows how the experiment was set-up. As previously described, the asteroid model is mounted on a geodetic tripod, which in turn is set upon a rotating base. The tripod is centred on the base by placing the legs into the evenly spaced smaller rings that were included on the larger outer ring on the base. There is an optical plummet placed on the top of the tripod, which means that the position of the centre of the tripod (the position of the asteroid mount) can both be levelled and verified to be exactly above the centre of rotation of the rotating base. This way the simulated orbit can be as close to circular as is possible in this set-up. Having the asteroid mounted at an angle, means that the distance from the stationary camera to the centre of the asteroid will vary, similar to an elliptical orbit. The bottom right image of Figure 4.1 shows the degree indicator (here it is shown as green for clarity, in the real set-up it is black) that is used to determine the rotation of the asteroid (more detail in Section 4.3).

The broad steps of the experiment are summarised below. The full experiment plan is included in Appendix B. Before the experiment can be executed, there are seven steps of preparation that need to completed. First, all the sensors need to be tested to check functionality and to determine how the sensor interface works (the types of cables needed, software to gather the measurements, etc.). In this case that meant interfaces and software for the camera, which will be explained in Section 4.4. Secondly, the environment needs to be prepared. Since the calibration should be performed

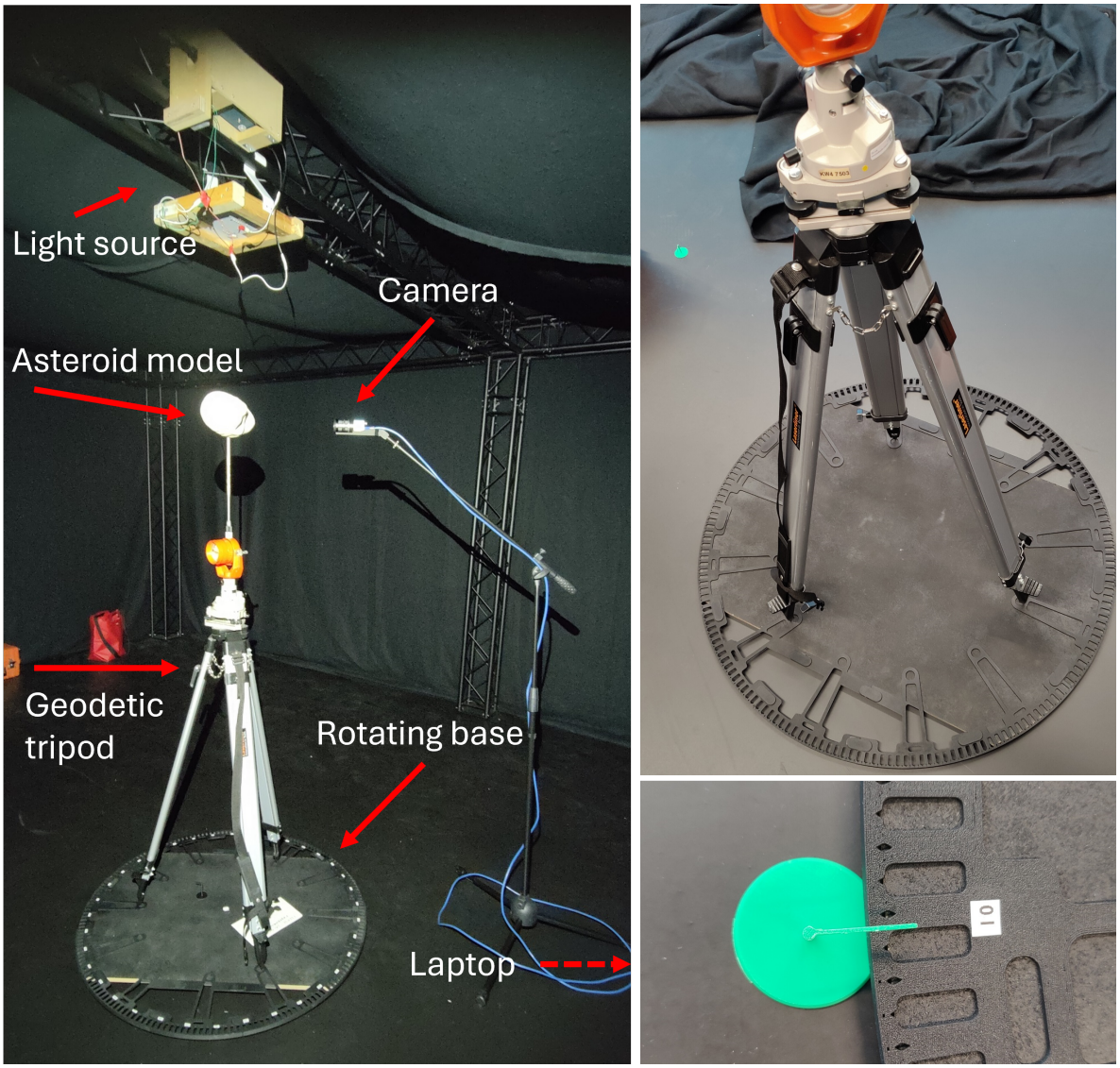

Figure 4.1: Left: Experiment set-up, all mayor components have been labelled and camera is set to simulate a 30 km orbit. Top right: Geodetic tripod centered and levelled on the base. Bottom right: Degree indicator is pictured at 0 degrees of rotation.

in experiment-like circumstances for it to be most accurate, mounts and lights should already be set-up, as shown in Figure 4.1. The lights will be elaborated on in Section 4.2. After the set-up is readied, the calibration can be completed as per steps four to seven. These calibrations will be detailed in the later sections.

Experiment preparation

1. Prepare sensors
2. Mount Sun-like lamp above the test set-up
3. Perform tuning lens aperture
4. Complete camera calibration using the MATLAB *Single Camera Calibrator App*
5. Verify the rotation accuracy of the base plate
6. Verify the camera position in the test set-up with respect to the asteroid and centre to rotation
7. Verify attitudes of asteroid and camera, to ensure they are aligned along the inertial axes

After all the preparations are completed, the experiment itself can be executed. The basic steps are detailed below.

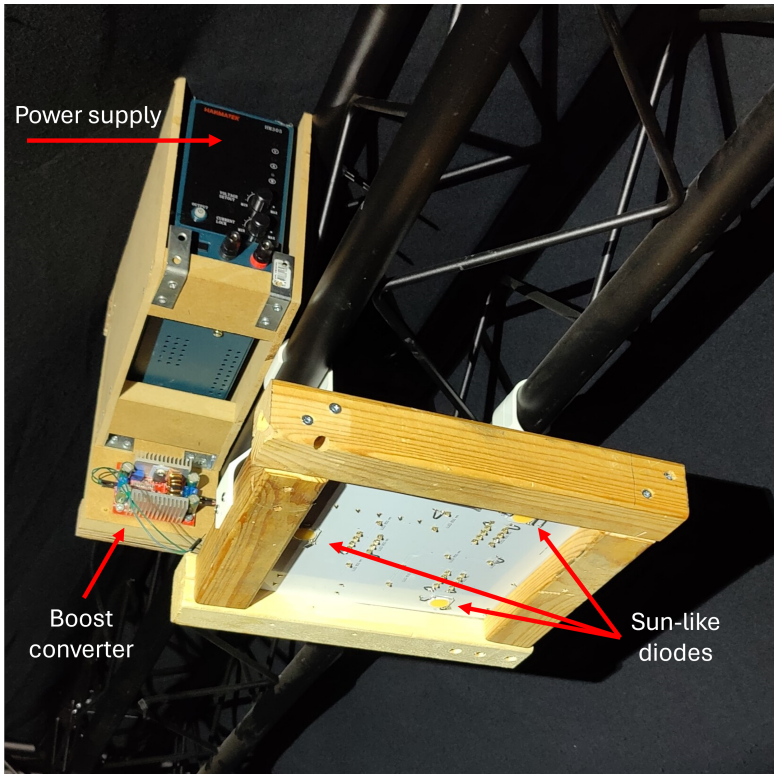

Figure 4.2: Light source used in the experiment. All the components are indicated in the image.

Experiment steps

1. Set ampere limit on the lamp
2. Set rotation to 0 degrees at the indicator flag
3. Set-up data management system
4. Turn on Sun-like lamp
5. Capture image
6. Verify image capture success
7. Rotate base 2 degrees
8. Capture image
9. Repeat until a full 360 rotation is completed, periodically turning off the lamp to avoid overheating.

4.2. Lighting

To make the sensor measurements reflect reality as much as possible, a Sun-like lamp was used. Figure 4.2 shows how the lamp was set-up in the experiment. A power supply was used to control the brightness of the lamp by limiting the current. The light-emitting diodes (LEDs)used in the lamp need 40 V to get to their full brightness, but the power supply can only output 20 V. To compensate a boost converter is used to get to the 40 V, at 5.1 A.

The measurements were conducted for two different lighting scenarios. For the first light scenario, the lamp was set to full brightness, at 5.1 A and 40 V. A challenge here was that the lamp would overheat. Therefore, measurements could be taken in 6 minute intervals with 3 minutes between the sets of measurements to allow the lamp to cool.

The second light scenario was with dimmed light. It was attempted to recreate real Eros images, and by limiting the lamp at 1.1 A a similar depth of shadow was created in the images. Thus, the power supply was limited at 1.1 A for the second set of measurements.

The intensity of the lamp and beam width of the light could not be matched to the true conditions around Eros within the limits of this experiment. The beam width of the 3 LEDs was too large compared to the beam width of the Sun at Eros, which means that the light on the surface of the model comes further around the equator and to the south pole. The shadows are more shallow due to this as well.

Even though multiple light sources were used, it was not observed that there were clear penumbra, or a shadow that was cast by one light source while being partially lit by another, creating multiple shadows with varying shades.

4.3. Rotation

To create images for a full orbit simulation either the asteroid or the sensors would have to move. As explained in Section 4.1 it was decided to have the asteroid rotate and to keep the sensors stationary. This was accomplished by using a large ring bearing and mounting the tripod holding the asteroid model on top.

To determine the rotation of the asteroid between each image, the conditions in a 30 km orbit are used since this is the fastest orbit of the orbits considered and will need the smallest angle between measurements. Assuming a navigation image is taken every 3 minutes, Eros will have rotated 3.42 degrees (for a rotational velocity of ω = $3.312 \cdot 10^{-4}$ rad/s) and the satellite will have turned 1.33 degrees (for an orbital velocity of V_c = 3.86 m/s) in that time. Therefore, the relative rotation of Eros compared to the satellite in 3 minutes is 2.09° $\approx$ 2°. Thus, the asteroid will be rotated by 2° between each measurement.

4.3.1. Rotating base design

The rotation was measured with a large ring that was marked for every half degree along the full 360° rotation. The ring was modelled in Autodesk Fusion, and 3D printed using the FDM printer P1P from Bambu Lab[1] with a standard black PLA (plant based polylactic acid plastic) filament. To account for the print limit of the printer the degree indication ring was printed in 12 pie slices, each spanning 30°, that were linked together. Additionally, there was a lip added to secure it to an MDF (medium-density fibreboard) base plate so it could not rotate independently of the tripod. Furthermore, at every sixth part of the circle a cut-out was added that could hold a foot of the tripod, so the legs could be evenly spaced. To read the measurements consistently, a small flag was stuck to the floor. One side of the flag had to be aligned to one the indicated degrees. Figure 4.1 shows the full ring and its location in the experimental set-up in the top right and left images. Here it is also visible where the tripod legs are positioned in the smaller rings included in the design. The bottom right image shows the indicator flag positioned at 0° rotation. The diameter of the ring was made as large as was feasible for the 3D printer volume, spanning 1 meter in diameter. A larger distance to the centre of rotation would make it possible to make small adjustments.

4.3.2. Calibration

To determine the accuracy of this method of measuring rotation, several calibration measurements were taken. The laser range finder (LRF) was mounted onto the geodetic tripod in place of the asteroid (see Figure 4.1) to measure the distance $R1$ to a point on a board the other side of the room. Next, the base was rotated by a set angle, and the distance $R2$ to the board was measured again. With these measurements and the distance s between the two points on the board, the actual angle the base rotated could be calculated with the law of cosines. Table 4.1 shows the measurements. Each measurement was completed three times and the rotation was measured six times, to reduce the chance of outliers. If one measurement varied more than a centimetre it was discarded and a new measurement was taken.

Table 4.2 shows the angle as indicated on the base and the angle that was calculated with the measurements. The error between the two was then scaled to the orbits used in the experiment, to quantify how far the estimate of the orbital position would be off. The resulting errors are at the scale of 10^2 m for the 30 km and 100 km orbit, which is within the 3σ range for along track navigation error requirement of 85 m for the OSIRIS-REx mission (Antreasian et al., 2022), and better than the 100 m navigation error for the Hayabusa2 mission (Tsuda et al., 2020) (see Section 2.1). Therefore, the error in the rotation measurement is small enough to not dominate potential navigation errors.

[1] https://eu.store.bambulab.com/en-nl/collections/3d-printer/products/p1p [Cited: 15-07-2024]

Table 4.1: Rotation accuracy calibration measurements. Every measurement was repeated three times and the rotations were repeated six times to increase statistical significance.

Meas.	$R1$ [mm]			Average [mm]	$R2$ [mm]			Average [mm]	s [cm]
1	3001.6	3003.1	3002.6	3002.4	3076.2	3075.5	3075.6	3075.8	53.70
2	3020.8	3020.4	3020.5	3020.6	3048.4	3048.0	3047.6	3048.0	31.78
3	3026.2	3026.3	3026.4	3026.3	3065.1	3064.8	3064.1	3064.7	32.10
4	3035.4	3035.2	3036.5	3035.7	3085.4	3085.7	3085.5	3085.5	32.45
5	3021.5	3021.8	3021.2	3021.5	3048.1	3048.4	3048.7	3048.4	31.85
6	3027.1	3027.0	3027.0	3027.0	3065.1	3065.2	3065.1	3065.1	32.25

Table 4.2: Resulting rotation angles calculated based on the measurements in Table 4.1. The resulting average error was scaled to full orbit to determine validity of the method to measure the rotation.

Meas.	set angle [deg]	meas angle [deg]	error [deg]	at scale 30km [m]	at scale 100km [m]	at scale 200km [m]
1	10.0	10.043	0.043	44.7	149.2	298.3
2	6.0	5.981	0.019	19.5	65.2	130.3
3	6.0	5.999	0.001	1.4	4.7	9.4
4	6.0	6.006	0.006	5.9	19.7	39.4
5	6.0	5.994	0.006	6.1	20.4	40.4
6	6.0	6.026	0.027	27.8	92.6	185.2
Average			**0.017**	**17.6**	**58.6**	**117.2**

4.4. Camera

To simulate optical navigation measurements, an optical camera was used. This section elaborates on which camera was used and its corresponding resolution was evaluated. The design of the mounting system used in the experiment is explained and the camera calibration is discussed.

4.4.1. Camera model

To simulate the navigation camera a readily available camera was used. The MER2-160-227U3C camera from Daheng Imaging[2] in combination with a LCM-5MP-08MM-F1.4-1.5-ND1[3] lens. The images were captured using the Galaxy Viewer[4] software, which is compatible with the Daheng camera.

From the documentation initial calculations were made in the literature review on the expected surface resolution in the experiment. These calculations are summarised in Table 4.3, for the lowest altitude in orbit around Eros. As mentioned previously in Subsection 3.1.1, the Hayabusa2 navigation camera would have a surface resolution 13.5 m at this altitude of 11.4 km. Comparing this with the expected resolutions stated in Table 4.3, the experiment camera has a similar resolution to the Hayabusa2 cameras. Therefore, the camera was deemed suitable for creating experimental optical navigation images.

Table 4.3: Surface resolution of the experiment camera at the lowest altitude above Eros, at the experiment scale and scaled up to true scale.

	30 km	100 km	200 km
1:1	0.098 mm	0.764 mm	0.961 mm
$10{:}1{\cdot}10^6$	9.83 m	76.45 m	96.08 m

[2]https://en.daheng-imaging.com/show-107-2031-1.html [Cited: 13-11-2024]
[3]https://www.get-cameras.com/LENS-C-mount-5MP-8MM-F1.4-2/3-LCM-5MP-08MM-F1.4-1.5-ND1 [Cited: 25-11-2024]
[4]https://en.daheng-imaging.com/list-59-1.html [Cited: 25-11-2024]

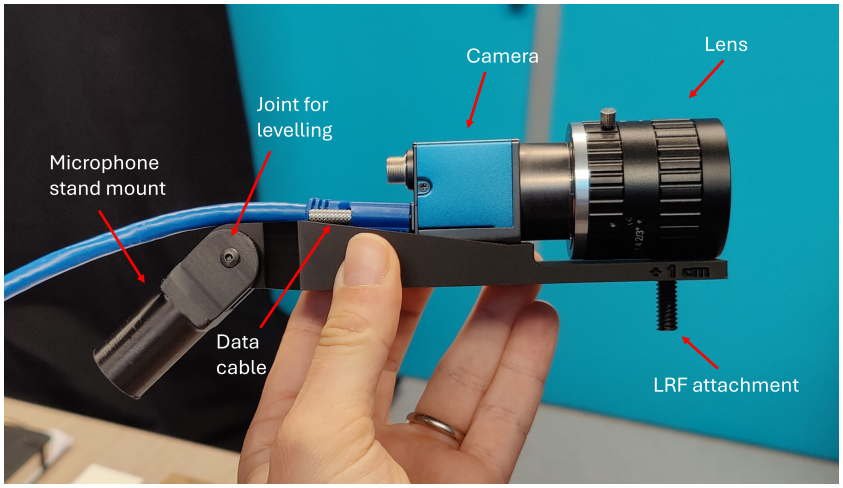

Figure 4.3: Camera attached to the mount.

4.4.2. Mount

To place the camera in the set-up, a mount was designed to attach the camera to a microphone stand with a 3/8 inch thread, as can be seen in Figure 4.1. The microphone stand gave the flexibility of being able to easily move the camera to the desired position and allowing the height of the camera to be adjusted. The mount itself has a joint that makes it possible to put the camera level with the equatorial plane of the Eros-model, the joint is indicated in Figure 4.3.

The camera is added to the top of the mounting plate with three screws which screw directly into the housing to facilitate a strong connection. At the front of the mounting plate a threaded hole is added with a 1/4 inch thread. This hole is located at the focal point of the camera according to the camera calibration (more on the calibration in the next subsection). The 1/4 inch thread allows a short 1/4 inch threaded rod to be inserted, onto which an LRF can be screwed. The LRF can measure from its mounting point, thus this way the distance from the focal point of the camera to the centre of the asteroid can be measured directly. In this experiment the Leica DISTO X3[5] was used.

4.4.3. Calibration

Before the experimental measurements were collected, the camera had to be tested calibrated. The two camera settings that had to be adjusted in Galaxy Viewer from default were:

```
Device>BalanceWhite>continuous
Common>ExposureTime>30000
```

Adjusting these two settings allowed the camera to capture a visible colour picture. If the white balance was not corrected for each lighting situation (which might change when moving the camera, or turning a lamp on and off) the white balance would be off. The exposure time had to be set high enough to allow the camera to capture enough light to get a properly exposed image.

Aside from the software settings, there were two sets of calibration that had to be completed. Selecting an appropriate aperture, and calibrating the camera to determine the focal length, pixel skew or distortion and the principal point (pp, the point on the image sensor where the optical axis crosses the image plane) of the image sensor.

Aperture The aperture of the lens that was used could be adjusted. The aperture settings determine how “open” the lens is and thus how much light it lets through. The aperture size is denoted with an F-stop number, which is the ratio of the focal length to the diameter of the aperture. A larger aperture means a small F-stop number and more light being let in. Additionally, a small F-stop number also leads to a more narrow depth of field, which means that the fore- and background become out of focus. Ideally in the experiment the F-stop should be as large as possible to ensure that the entire asteroid is

[5] https://shop.leica-geosystems.com/sites/default/files/2020-01/Leica_DistoX3_UM_nl.pdf?srsltid=AfmBOor5Rq4WPGJya3UrrlkCiNLNOtajKkIVcyeAruaOVGpVCQu5mtlq [Cited: 13-11-2024]

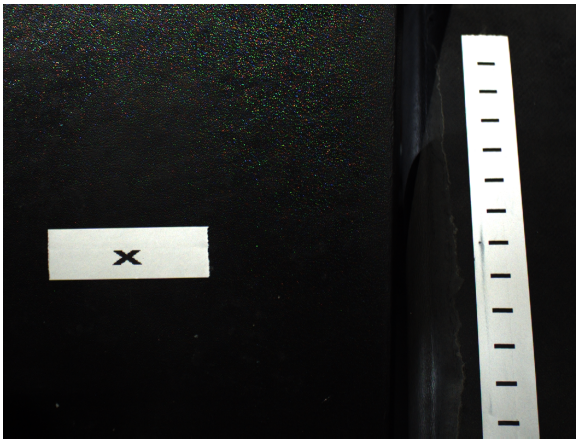

(a) Focus for small F-stop

(b) Focus for maximal F-stop

(c) Focus for final aperture setting

(d) Final aperture setting on lens, F-stop ≈ 7.8

Figure 4.4: Different F-stop options for aperture settings. Bottom row shows final setting.

seen in focus. However, a large F-stop and thus less light being let in, also means that longer exposure times are necessary to capture the image. Longer exposure times can lead to more noise on the image and it can cause the image to be less “sharp”. Therefore the correct aperture setting for the experiment had to be found.

To find the appropriate F-stop on the lens, a point and a ruler were positioned in front of the camera. The point was set in the middle of the image and used as the focus reference. The ruler was set next to the point, angled backward at roughly a 30 degree angle from vertical and making sure that the centre of the ruler is set at the same distance from the camera as the reference point. By increasing the F-stop, it can be observed at which point the closer end of the ruler and the further end go from out of focus to in focus.

Figure 4.4 shows the reference point (the “x”) and the ruler. Figure 4.4a was taken with a small F-stop. The reference point is in focus, but the along the top of the ruler it can be seen that the last lines are not. Figure 4.4b is an example of using the largest F-stop - 16. Since the aperture diameter was so small a long exposure time was needed to capture the image, which caused the blurriness. The bottom row of Figure 4.4 shows the final selected F-stop of approximately 7.8 and the calibration image. There is still some slight difference in focus along the ruler, however this was the best balance

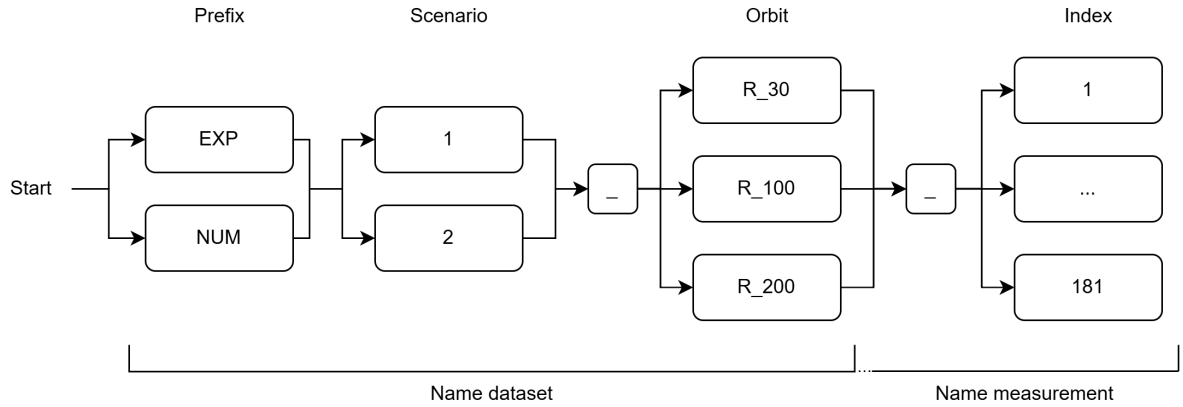

Figure 4.5: Flowchart for the naming convention of the datasets and the measurements.

for a larger depth of field without having to increase the exposure time to the point of losing the focus on the reference point.

Image sensor calibration To complete this calibration, the MATLAB Camera Calibrator[6] app was used, with a checkerboard[7] calibration pattern. Using the experimental set-up with both lighting conditions, and at a simulated 30 km orbit and 200 km orbit, four sets of images were captured with the camera. Each set had enough images to cover the full image frame and at varying incidence angles (no more than 45° from the vertical). For the 30 km orbit this took around 13 images and for the 200 km it took around 25 images. These images were used as the inputs by the calibrator app, together with the exact dimensions of the checkerboard squares.

The calibration algorithm used by the calibrator app assumes a pinhole camera model. By identifying the checkerboard in the images, the intrinsic and extrinsic camera parameters, and the distortion coefficients can be estimated using a Levenberg-Marquardt nonlinear least-squares minimisation[8]. Since the exact dimensions of the checkerboard are known, any distortion in the relative sizes of the squares is due to any lens distortions. From the calibration the most important outputs are the location of the pp, the estimated focal length, and the skew and distortion coefficients, which indicate how much an image is deformed by the camera and how. For more details on the calibration the reader is referred to the MATLAB documentation[9].

The results from the calibration are included in Appendix C. The estimated focal length was used to measure the distance between the focal plane and the centre of rotation in the experimental set-up, to get the simulated orbit as close as possible to the theoretical distance. The distortion coefficients were all zero, or close to zero. This means that for the calibration no significant lens distortions were present.

4.5. Description of measurements

In total, five data sets were created in the experiment. The two lighting scenarios discussed in Section 4.2 were applied to the simulated orbits of 30 and 200 km, creating four datasets. Lighting scenario 1 indicates the lights set to their maximum brightness, and scenario 2 is for the limited brightness. When it became apparent that the depth of field was not large enough for the 30 km orbit, a fifth dataset was created at the orbit of 100 km. This was the furthest distance from the model where the lens did not need to be refocussed due to the narrow depth of field. This orbit was only imaged for scenario 2, since the measurements from EXP2_R_30 and EXP2_R_100 were more similar to the images of Eros from the NEAR mission in terms of how the light was reflected off of the model, than was the case for the EXP1 datasets.

[6] https://nl.mathworks.com/help/vision/ref/cameracalibrator-app.html [Cited: 13-11-2024]
[7] https://nl.mathworks.com/help/vision/ug/calibration-pattern-and-properties.html [Cited: 13-11-2024]
[8] https://nl.mathworks.com/help/vision/ug/using-the-single-camera-calibrator-app.html [Cited: 05-12-2024]
[9] https://nl.mathworks.com/help/vision/ug/camera-calibration.html [Cited: 05-12-2024]

4.5.1. Numerical dataset

Aside from the experimental measurements, six more datasets were created using Blender, a 3D modelling software. The use of Blender allowed the experimental measurements to be recreated without sensor errors. By comparing the experimental measurements to the numerical measurements, the numerical measurements could be used as a benchmark to determine the quality and errors of the experimental measurements.

These numerical datasets did not contain 181 measurements, instead a measurement was made every 20 degrees instead of every 2 degrees. Since the experimental set-up was not needed for these measurements, they could be generated efficiently and if more were required they could be created on demand. The images were compared manually, limiting the number of measurements that could be compared. At this time 19 numerical measurements per dataset were considered sufficient.

The 3D model on which the 3D printed asteroid of Eros was based, was loaded into Blender and rendered with linear light without atmospheric refractions, to simulate the lighting at Eros as close to real as possible, the Blender shading and camera settings are detailed in Section B.2. For the numerical datasets there were two different scenarios as well. Here it was not the lighting that varied, but the rendering method. The NUM1 dataset is rendered with the 3D model as is, which means that all the edges and vertices are visible in the final render. The NUM2 dataset was created with the "shade smooth"[10] function in Blender, which renders smooth, rounded surfaces over the straight lines of the edges and vertices. However, for simplicity only the NUM1 dataset will be used for the analysis.

4.5.2. Measurements discussion

When creating the datasets there were several limitations in how the experiment was set-up, which may influence the accuracy of the dataset. These limitations need to be considered during the analysis in Chapter 5. The two main points are uncertainties in the focal length of the camera, and mistakes and limitations in the set-up. Firstly, the focal length was calibrated before the experiment and therefore known at that specific point in time. However, as mentioned the measurements at the 30 km orbit radius were taken, the focus of the camera had to be adjusted due to the limited depth of field. By adjusting the focus of the lens used in the experiment the focal length can change. Therefore, the focal length for each of the datasets is not exactly known. Any calculations performed later in this work will use the results from the camera calibration, but this uncertainty should be considered.

Secondly, there were several limitations on the experimental set-up, that became apparent after the measurements had been completed. The most important mistake that was made, was that the LRF used in the experiment can measure from its bottom, its mounting point (which was used in the experiment) or its front. Initially the LRF was tested to verify which distance it measured. However, what was overlooked was that all settings on the LRF revert to default after it is restarted (Leica Geosystems, 2020). The default measurement state of the LRF is to measure from the bottom of the device, which is a difference of 1.0 cm. Thus, all measurements taken to verify the position of the camera in the experimental set-up are 1 cm shorter in reality. The calibration measurements detailed in Table 4.1 have been corrected for the 1 cm difference. In the experiment itself, 1 cm is equal to a 1 km change in the orbital radius.

Aside from the mistake made with the LRF, a limitation of the experiment is that the position of the asteroid and the camera in the set-up could not be captured. Therefore, the numerical dataset that was created could not be made to match the experimental set-up exactly, as the orientation of the asteroid at a rotation of 0 degrees, or index 1, was not known. The orientation was recreated manually by eye, but the numerical and experimental measurements might have a difference in their rotation in the respective datasets. The same is true for the camera position. The numerical datasets were created before the mistake in the distance measurements was known and therefore do not include a correction.

The laboratory where the experiment was performed has since been equipped with a motion tracking system, which in the future might be used to map the positions of all the components of the experiment. These positions can then be recreated more accurately in a numerical model used for verification, or be referred to later. Additionally, the use of robotics might reduce these errors as these can be programmed in advance to be positioned at an exact location relative to a reference point.

[10] https://docs.blender.org/manual/en/2.91/scene_layout/object/editing/shading.html [Cited: 26-11-2024]

5

Dataset analysis

After the experiment has been completed, the created datasets are processed to create position estimates for the camera, or simulated spacecraft. These results can be used to evaluate the quality of the data and how such an experiment can be applied in further research on navigation algorithms. In Section 5.1 the theory behind the position estimate is discussed, after which results are evaluated in Section 5.2. Section 5.3 considers the causes to any errors that might be present in the results by quantifying the bias, human error and uncertainties due to the experimental set-up. Some other possible applications of the experiment are examined in Section 5.4 and finally a summary of the findings in this chapter is given in Section 5.5.

5.1. Theory

Now that the dataset of images has been created, the next step is to evaluate the quality of the dataset. The metric used to assess the experimental measurements is the error in the estimation of the camera position based on the images. Several landmarks are selected, of which the positions in the inertial coordinate system (refer to Chapter 2) are known. These landmarks are then localized in the images, for both the experimental and numerical images. Based on these points, the location of the camera can be calculated. A perfect image, where all the landmarks can be identified with zero uncertainty, will lead to the correct camera position. Therefore, the difference in the estimated camera position $\mathbf{p}_{c,e}$ between the experimental and the numerical datasets, and the true solution $\mathbf{p}_{c,t}$, will give insight into how accurate the experimental measurements are.

Figure 5.1 shows how some landmarks might be selected in an image from the dataset. Section D.2 contains images from the dataset with landmarks for reference. The position of each point is initially given in pixels from the top left corner of the image. The principal point (pp) is the point on the image sensor, where the optical axis crosses the image plane. To be able to calculate the camera position, which lays along the optical axis, the coordinates of each of the points are corrected to their position with respect to the pp. The x and z coordinates of point p1 as shown in the image, are the coordinates after this correction. Having determined the coordinates, the camera position can be calculated for any set of three or more points.

The process of finding the camera position is visualised in Figure 5.2. Figure 5.2a shows the basic principle under the assumption of a pinhole camera. The relative position of the points with respect to the camera can be described with vectors that have the respective lengths d_N, for each of the N points. The point of intersection of these vectors is the location of the camera. However, the magnitude and direction of these vectors is unknown when the camera position is unknown, but using Equation (5.1), which expresses the point of intersection, the camera position estimate $\mathbf{p}_{c,e}$ can be calculated.

$$\hat{\mathbf{u}}_1 d_1 + \mathbf{p}_1 = \hat{\mathbf{u}}_2 d_2 + \mathbf{p}_2 = \cdots = \hat{\mathbf{u}}_N d_N + \mathbf{p}_N = \hat{\mathbf{u}}_{c,e} d_{c,e} = \mathbf{p}_{c,e} \tag{5.1}$$

Considering Figure 5.2b, the image can give the direction of the vectors needed to solve Equation (5.1) for d_N. $\mathbf{r}_N$ is the location of the point in the image seen from the camera. As mentioned, the x and z coordinates are measured from the pp, and the y coordinate is the focal length. Normalising

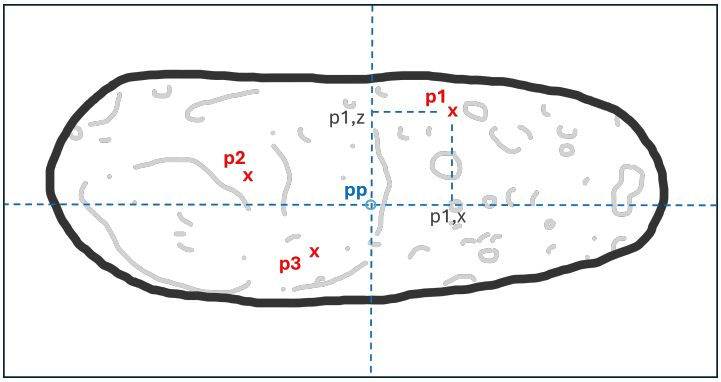

Figure 5.1: Visualisation of selected points in image from dataset. Coordinates of points are given relative to the principle point.

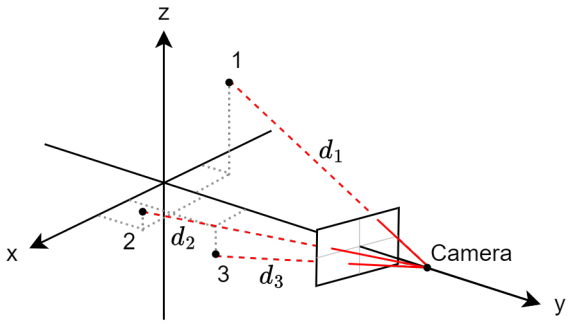

(a) Points P1, P2 and P3 at each distance *d* from the camera, which is located on the y-axis.

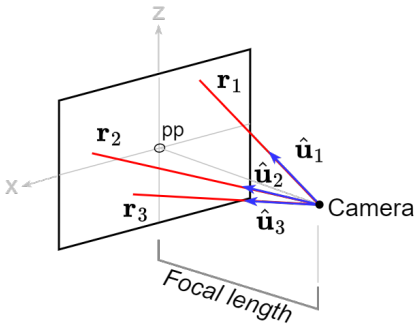

(b) The unit vectors in the directions of each of the points can be extracted from the image. x and z coordinates are based on the pixel coordinates, and the y coordinate is the focal length.

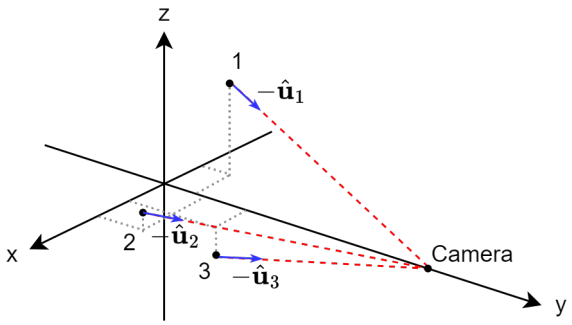

(c) Intersection of the three vectors from points at the location of the camera, using the unit vectors for direction, and distance *d* for the vector magnitude

Figure 5.2: Visualisation of the three steps needed to calculate the camera position based on the relative positions of the point P1, P2 and P3 with respect to the camera in the inertial reference frame.

these vectors gives the unit vectors $\hat{\mathbf{u}}_N$ which describes the direction to the N points from the camera, thus only the magnitude of these vectors is unknown.

By reversing the unit vector as seen in Figure 5.2c and defining its origin at the points $\mathbf{p}_N$, the problem described the location of the intersection in the inertial frame. This linear set of equations can be expressed as the following least squares problem (Blobel, 2005):

$$\mathbf{Ax} \approx \mathbf{p} \tag{5.2}$$

Matrix $\mathbf{A}$ and vector $\mathbf{p}$ are described in Equation (5.3a) and the solution to the magnitudes d_N and the approximate position of the camera is calculated in Equation (5.3b).

$$\mathbf{A} = \begin{bmatrix} \mathbf{I}_3 & -\hat{\mathbf{u}}_1 & \mathbf{0}_{3x1} & \dots & \mathbf{0}_{3x1} \\ \mathbf{I}_3 & \mathbf{0}_{3x1} & -\hat{\mathbf{u}}_2 & \dots & \mathbf{0}_{3x1} \\ \vdots & \vdots & \vdots & \ddots & \vdots \\ \mathbf{I}_3 & \mathbf{0}_{3x1} & \mathbf{0}_{3x1} & \dots & -\hat{\mathbf{u}}_N \end{bmatrix}, \quad \mathbf{p} = \begin{pmatrix} \mathbf{p}_1 \\ \mathbf{p}_2 \\ \vdots \\ \mathbf{p}_N \end{pmatrix} \tag{5.3a}$$

$$\mathbf{x} = \left(\mathbf{A}^\mathsf{T}\mathbf{A}\right)^{-1}\left(\mathbf{A}^\mathsf{T}\mathbf{p}\right) = \begin{pmatrix} \mathbf{p}_{c,e} \\ d_1 \\ \vdots \\ d_N \end{pmatrix} \tag{5.3b}$$

The inverse in this equation was calculated with the MATLAB *mldivide* function, which uses a QR solver for non-square matrices[1] as is the case for $\mathbf{A}$ while $N \neq 4$.

The method was verified using the trilateration method developed by Norrdine (2012), which uses a least squares regression on a similar linear system, using his code (Norrdine, 2018) to compare the results. For the test cases there was only a numerical difference between the two solutions of 10^{-6}. The numerical error of the method itself is in the order of magnitude of 10^{-11}.

The covariance matrix of the solution and the correlation matrix can be calculated by using Equation (5.4) and Equation (5.5).

$$\mathbf{r} = \mathbf{p} - \mathbf{A}\mathbf{x} \tag{5.4a}$$

$$\sigma^2 = \frac{\|\mathbf{r}\|^2}{n-p} \tag{5.4b}$$

$$\text{Cov}\left(\mathbf{x}\right) = \sigma^2\left(\mathbf{A}^\mathsf{T}\mathbf{A}\right)^{-1} \tag{5.4c}$$

The covariance can be used to calculate the variance for each of the variables and to gain insight in how much the variables change in relation to each other, their covariance. The diagonal of the covariance matrix holds it variable its variance and the other element the respective covariances of variables i and j. To find the covariance matrix first the residual $\mathbf{r}$ of the estimate is calculated, with which the variance σ^2 can be determined by dividing the square of the magnitude of the residual by the difference in its dimensions n, the width of $\mathbf{r}$, and p, the height of $\mathbf{r}$. The covariance matrix of $\mathbf{x}$, the estimate, can then be found with Equation (5.4c).

From the covariance matrix, the correlation matrix can be found using

$$\text{Corr}\left(\mathbf{x}\right)_{ij} = \frac{\text{Cov}\left(\mathbf{x}\right)_{ij}}{\sqrt{\text{Cov}\left(\mathbf{x}\right)_{ii} \cdot \text{Cov}\left(\mathbf{x}\right)_{jj}}} \tag{5.5}$$

The correlation shows how much each of the variables correlate to each other and the final estimate. If two variables are negatively correlated, the value of one increases as the value of the other decreases. Also, the higher the correlation, the stronger the variables influence each other with a correlation of 1 being the highest possible correlation. Equation (5.5) shows how each element i, j can be calculated from the covariance matrix.

A limitation of the method described in this section, is that it assumes the optical axis is parallel to one of the axes of the inertial reference frame. No rotation of the focal plane was included in the conversions to unit vectors, since an initial estimate of the position in necessary to determine the angle of the focal plane to any of the axes. For this research this method suffices, as the simulated orbits were equatorial and assumed to be aligned with the y-axis. The main question is the *quality* of the dataset. In the future the methods can be expanded to a more realistic scenario; both in the execution of the experiment and the methods with which the position estimate is calculated.

Additionally, the method of least squares indicated in Equation (5.2) is an ordinary least squares (OLS) solution. An OLS minimises the sum of the squared residuals. This means that no extra weights are given to the largest or smallest residuals. Therefore, the OLS is not robust to outliers, as it cannot "recognise" an outlier and adjust its solution to converge on the points with smaller residuals. Because of this, the final estimate $\mathbf{p}_{c,e}$ can diverge due to errors in individual points. Due to time constraints the OLS was not changed to a weighted least squares solution, or another method to make it more robust, though changing the least squares method could be done in future research.

[1] https://nl.mathworks.com/help/matlab/ref/double.mldivide.html [Cited: 09-12-2024]

Table 5.1: Average estimated position of the camera, for all datasets, orbits and sampled rotations. The norm of the difference in the estimated and true positions was calculated, and the number of points N for each estimate is given. The index links each result to their respective image in the dataset by the naming convention. Results without 1 km range correction.

Case	$x_{c,e}$ [m]	$y_{c,e}$ [m]	$z_{c,e}$ [m]	$\lvert\mathbf{p}_{c,t} - \mathbf{p}_{c,e}\rvert$ [m]	Orbit [km]	Rotation [°]	Index	N
EXP2	-1870.837	-26941.540	-1042.135	3733.665	30	0	1	8
	730.187	-25429.824	-767.337	4691.320	30	140	71	8
	966.232	-28006.511	-1137.184	2490.138	30	240	121	10
	-1559.823	-96679.839	-1828.497	4098.771	100	0	1	9
	906.603	-95467.597	-1804.528	4961.948	100	120	61	10
	860.738	-96123.823	-1699.683	4319.091	100	260	131	9
	755.935	-196697.942	-6400.553	7241.692	200	0	1	9
	2864.874	-189359.995	-5833.624	12467.894	200	120	61	10
	3034.341	-190631.012	-5642.490	11350.016	200	260	131	9
NUM1	24.502	-29909.630	-101.791	138.306	30	0	1	8
	50.265	-29641.044	-14.934	362.766	30	140	71	8
	9.794	-30433.066	-91.669	442.770	30	240	121	10
	115.466	-100068.522	-377.848	400.994	100	0	1	9
	109.871	-99508.900	-353.203	614.820	100	120	61	10
	76.140	-99638.392	-301.215	476.747	100	260	131	9
	249.737	-198311.656	-698.319	1844.051	200	0	1	9
	241.099	-198043.768	-692.374	2089.104	200	120	61	10
	241.242	-195316.198	-537.906	4720.757	200	260	131	9

5.2. Results

The method described in the previous section works for any set of three points. However, if one of those three points contains a large error than the error in the camera position estimate will also be large. It will be harder to evaluate the quality of the points since it will be hard to isolate the point with the deviation. By using more points any errors will weigh less in the solution and if only one point deviates strongly, it can be identified more easily. Table 5.1 shows the N number of points $\mathbf{p}$ that were chosen as landmarks for each case to estimate the camera position $\mathbf{p}_c$, the position of these points can be found in Section D.1. Note, these calculations were performed before the 1 km error due to the laser range finder (LRF) was found, as discussed in Section 4.5. The error is approximately 1 km smaller when the results are compared to a perfect camera position located at the orbital radius minus 1 km. The error does vary by around 5-10% and the exact correction is not known. Due to time constraints the calculations could not be redone. Therefore, the original values are left in the table, with the note that the actual error should be around 1 km less.

Each of the points are identified manually in the images. To further increase the robustness of the estimate, the landmark identification is repeated ten times, leading to ten estimates of $\mathbf{p}_c$ of which the average is used in the evaluation of the data. This reduced human error in the landmark identification. Figure 5.3 shows the selected points of ten instances around the pp. The average results on the camera position estimate are given in Table 5.1, for several simulated orbital positions at all examined orbits.

In Figure 5.3 it can be observed that the EXP2 points are off from the “true” position of the points. The true position is calculated by first finding the vector $\mathbf{d}$ between the points to the camera:

$$\mathbf{d} = \mathbf{p} - \mathbf{p}_c^{\mathsf{T}} \cdot J_{Nx3} \tag{5.6}$$

which is then normalised with respect to the y coordinates and multiplied by the focal length, to scale the points to their position on the focal plane. In principle, it is the reverse approach to finding the camera position as described in Section 5.1. This explains why the true position for the NUM and EXP points are not in the same position, since the focal length for the NUM datasets were set to 8.6 mm as an average for the different cases, and the EXP2 dataset was set to the focal length for the R_30 case at 8.56 mm, as can be seen in Appendix C. There is also a difference in the pixel size for the NUM ($2.604 \cdot 10^{-6}$ m) and the EXP ($3.45 \cdot 10^{-6}$ m) images, but by expressing the landmark positions in mm instead of pixels, this difference is accounted for (see Figure 5.3b). This does not eliminate the large difference in EXP2 to the expected positions of the points. Table 5.1 also shows a large error for

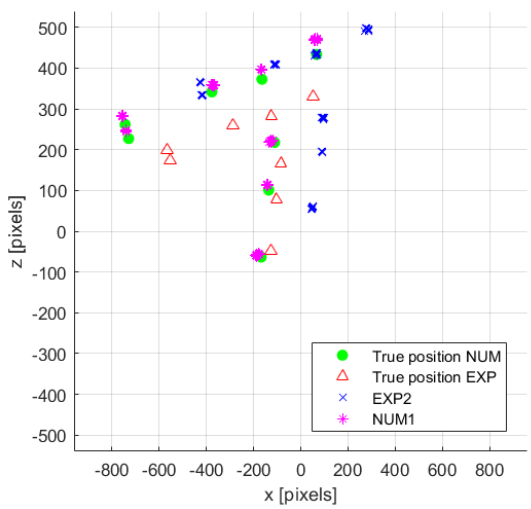

(a) Selected points for orbit 30 km, at 0 degrees rotation. True locations are given based on a projection of the known positions of the points around the principle point.

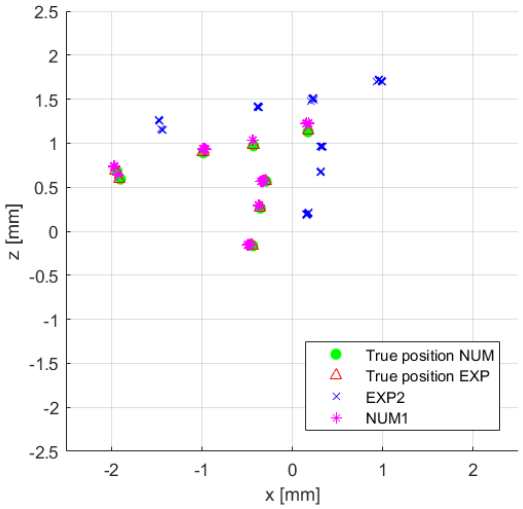

(b) Selected points for orbit 30 km, at 0 degrees rotation. The locations in pixels are reverted to meter distance from the principle point to negate the difference in pixel size between the NUM and EXP images.

Figure 5.3: Location of manually selected points from EXP2_R_30_1 and NUM1_R_30_1.

the EXP2 case. The large values for estimated camera position in x, $x_{c,e}$, and z, $z_{c,e}$, explain the large position error since the true position of the camera is on the y-axis, so the expected values of $x_{c,e}$ and $z_{c,e}$ lie closer to 0. Looking at the results for all cases, not just R_30_1, shows that the large x and z values occur for each.

5.3. Errors and uncertainty

There are several options as to why the x-coordinate $x_{c,e}$ and z-coordinate $z_{c,e}$ of the estimated camera position deviate more than expected and why the total error between the estimate $\mathbf{p}_{c,e}$ and the true $\mathbf{p}_{c,t}$ camera positions is still in the range of kilometres. A bias in the EXP dataset, human error in the landmark selection and uncertainties in the experimental set-up. The following subsections investigate the different options and elaborate on other uncertainties present in the datasets.

5.3.1. Bias

Closer examination of the data points, as seen in Figure 5.3 for all cases, shows a consistent offset in the EXP2 points. Considering the limitations to the experimental set-up discussed in Section 4.5, the most likely cause of this offset is that the rotation axis in the EXP2 images does not line up to the same position with respect to the pp as is the case for the NUM1 images. This is supported by the fact that the position of Eros is not same in the EXP2 and NUM1 images. The location of all the points on the surface of Eros is taken with respect to its centre of rotation. By not having the centre of rotation along the optical axis in the EXP2 datasets, the inertial coordinate system and the camera's internal coordinate system (in which the unit vectors are determined) do not line up. To correct for this, the bias of the measurements was calculated, by confirming that the EXP2 results had a constant offset to the true points for the different indices. Figure 5.4 shows the differences in the errors in the estimated position with respect to the expected results.

The error in the NUM1 points is close to a full order of magnitude smaller compared to the EXP2 results, as can be seen in Figure 5.4. The magnitude of the error decreases with increasing orbit, which can be explained by the fact that a constant offset in the rotation axis is relatively smaller at larger orbits. Furthermore, for EXP2 the increase in error might be explained by the combination of the selection of landmark coordinates and the matching of the rotations. The "true" landmark coordinated were found using Blender. The landmarks selected in the images, were found on the surface of Eros in Blender, which could give the position of the points in "global" (meaning inertial) coordinates. It is possible that some of these points were wrongly identified in Blender. Although then the same increase in error would be expected at 100 km orbit, since those datasets used the same landmarks.

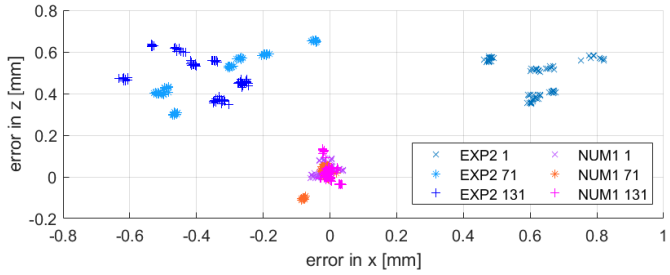

(a) Bias results for all indices investigated at R_30, for NUM1 and EXP2

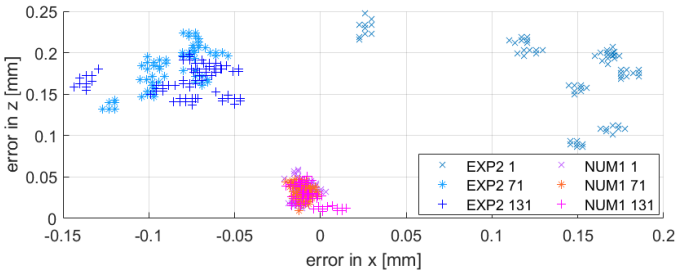

(b) Bias results for all indices investigated at R_100, for NUM1 and EXP2

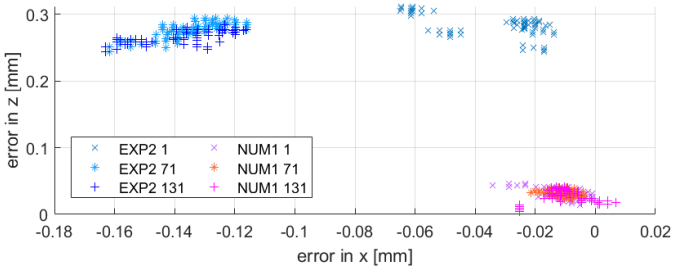

(c) Bias results for all indices investigated at R_200, for NUM1 and EXP2

Figure 5.4: Bias results for all orbits and analysed indices. The error is the difference in position for each selected point to their respective expected position according to the true solution.

Table 5.2: Bias correction applied to the initial location of the points identified in the images, to correct for the misalignment of the rotation axis of the asteroid in the images from the different datasets.

x_{EXP2} [mm]	z_{EXP2} [mm]	x_{NUM1} [mm]	z_{NUM1} [mm]	Orbit [km]	Index
0.61307	0.48672	-1.11825e-2	3.70690e-2	30	1
-0.34755	0.48355	-2.15127e-2	1.22857e-2	30	71
-0.38087	0.48813	-3.58296e-3	2.17275e-2	30	121
0.13914	0.17447	-1.01307e-2	3.31000e-2	100	1
-8.67175e-2	0.18253	-1.01957e-2	3.27949e-2	100	61
-7.76304e-2	0.16702	-6.56808e-3	2.84142e-2	100	131
-3.34588e-2	0.28395	-1.10842e-2	3.15056e-2	200	1
-0.13431	0.27635	-1.10751e-2	3.18060e-2	200	61
-0.13768	0.26455	-9.92395e-3	2.72900e-2	200	131

The matching of rotations was previously discussed in Section 4.5. Since the exact position of the camera and the orientation of the asteroid are unknown, it is possible that some difference in the rotation still exists between EXP2 and NUM1. The Blender coordinates were found based on the NUM1 rotation. Therefore it is possible that the positions of the landmarks with respect to each other, and their "true" position in the inertial frame is different for EXP2, which could lead to a different $\mathbf{p}_{c,e}$ in turn. In the future the experiment might be extended to include a mapping phase. By mapping the landmarks their position on the surface will be directly tied to the experimental set-up, reducing the uncertainties or unknowns when comparing the numerical and experimental datasets.

Table 5.3: Average estimated position of the camera after bias correction, for all datasets, orbits and sampled rotations. Results before 1 km range correction.

Case	$x_{c,e}$ [m]	$y_{c,e}$ [m]	$z_{c,e}$ [m]	$\lvert\mathbf{p}_{c,t} - \mathbf{p}_{c,e}\rvert$ [m]	Orbit [km]	Rotation [°]
EXP2	-271.504	-27004.625	217.504	3015.509	30	0
	-21.817	-26453.649	263.442	3556.190	30	140
	-8.087	-26721.025	198.097	3284.963	30	240
	-35.797	-96524.663	87.947	3476.634	100	0
	-10.983	-96473.848	118.227	3528.150	100	120
	29.624	-95391.818	121.385	4609.875	100	260
	-1.699	-196745.580	34.732	3254.605	200	0
	-25.094	-192851.687	103.812	7149.111	200	120
	41.514	-188168.379	164.238	11832.833	200	260
NUM1	-8.143	-29911.204	6.745	89.423	30	0
	-5.956	-29730.924	13.236	269.467	30	140
	-0.219	-30405.197	-28.032	406.165	30	240
	1.209	-100084.459	-4.125	84.568	100	0
	-2.113	-99646.295	7.190	353.784	100	120
	3.582	-99562.308	17.356	438.051	100	260
	-2.346	-198323.216	18.218	1676.884	200	0
	-7.071	-198371.859	20.857	1628.290	200	120
	21.170	-195127.840	72.238	4872.742	200	260

From this bias, a correction was calculated by determining the shift for each set of landmarks to bring the optical axis in line with the y-axis (see Table 5.2). A small change in the NUM1 results can also be observed, in the order of individual pixels, possibly due to a small misplacement of the camera in Blender. After applying the correction to the points, a new position estimate was calculated. The new results can be seen in Table 5.3. The largest effect of the bias correction is on $x_{c,e}$ and $z_{c,e}$. On average, there is a 95% decrease in the magnitude of $x_{c,e}$ for both EXP2 and NUM1, and an 86% decrease for $z_{c,e}$. Since these coordinates are zero for the true camera position, the bias correction does bring the estimate closer to the true position. There is no significant improvement for $y_{c,e}$ as there is only a 0.04% difference in the y coordinate estimate (Appendix D, Table D.2 has the differences for all orbits and indices). The relative distances between all points in the image do not change, only their positions with respect to the pp. The intersection between all vectors $\mathbf{d}$ will remain at a similar distance to the centre of the inertial reference frame. This was corroborated by the correlation matrix, as the correlation between the points used in the estimation and $y_{c,e}$ did not change.

The errors in the 200 km orbit are still several times larger (for EXP2 and NUM1 around 3 and up to 10 times, respectively) compared to the lower orbits. This might be due to increased difficulty in identifying the landmarks, although there is no greater variance to the selected landmark locations than for the lower orbits. A possible explanation could be due to the landmarks being closer together in the image. The vectors $\mathbf{r}_N$ will be more similar in length and direction and therefore a similar error will lead to a greater effect on $\mathbf{p}_{c,e}$ compared to the lower orbits.

Figure 5.5 shows how the estimate of the camera position was corrected to lay along y-axis after the bias correction. Again, the landmark locations are expressed both by the pixel position and in mm to adjust for the difference in pixel size. It should be noted, that the bias correction only moves the points with respect to the pp, which means that any error in perspective due to a different position of the camera is not corrected. The bias correction can only be used to make slight adjustments to correct for the optical axis being slightly off from the desired point of view. For large adjustments the respective positions of all the points in the image would have to be adjusted to change along with the change in perspective. However, that would mean recalculating the entire dataset numerically, which takes away from the goal of this experiment of evaluating the quality of the datasets collected in an experiment.

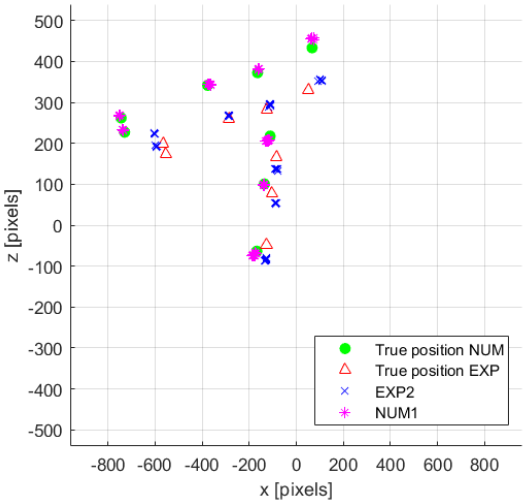

(a) Selected points for orbit 30 km, at 0 degrees rotation after the bias correction.

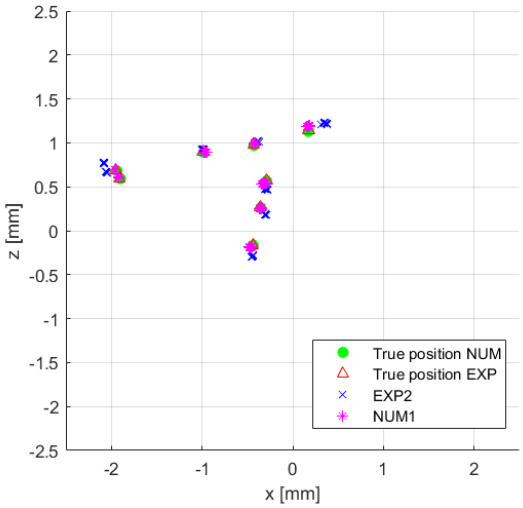

(b) Selected points for orbit 30 km, at 0 degrees rotation after the bias correction. The locations in pixels are reverted to meter distance from the principle point to negate the difference in pixel size between the NUM and EXP images.

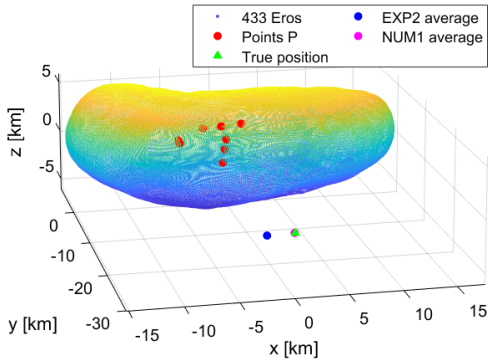

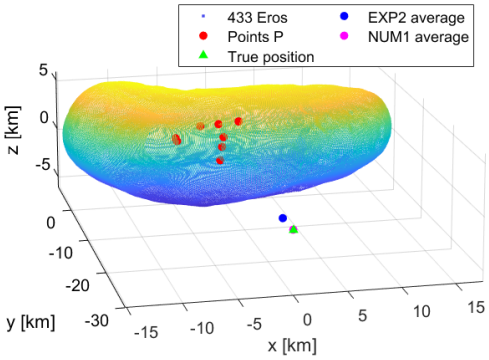

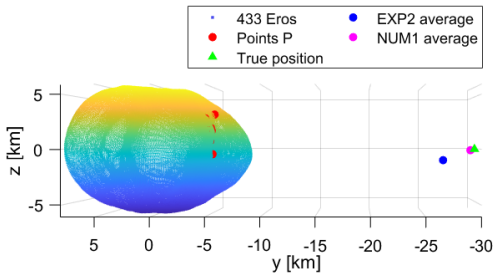

(c) Average estimated camera positions for EXP2 and NUM1 at R_30_1 before bias correction.

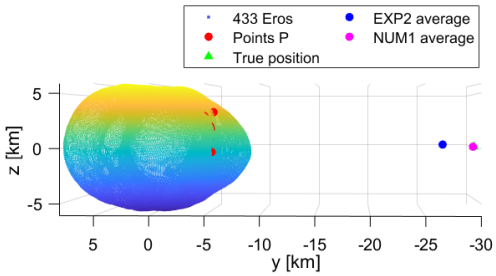

(d) Average estimated camera positions for EXP2 and NUM1 at R_30_1 after bias correction.

Figure 5.5: Comparison between the camera position estimates for the EXP2 and NUM1 datasets at R_30_1, before and after bias correction. Estimate aligns to y-axis after the correction.

Table 5.4: Error in camera position estimate when a pixel error is applied to the points used to estimate the position.

Orbit [km]	e_x [px]	EXP $e_{\mathbf{p},c}$ [m]	NUM $e_{\mathbf{p},c}$ [m]	e_z [px]	EXP $e_{\mathbf{p},c}$ [m]	NUM $e_{\mathbf{p},c}$ [m]	$e_{x,z}$ [px]	EXP $e_{\mathbf{p},c}$ [m]	NUM $e_{\mathbf{p},c}$ [m]
30	1	14.022	10.658	1	10.087	7.667	1	17.117	13.011
	2	28.044	21.317	2	20.175	15.335	2	34.235	26.022
	3	42.067	31.975	3	30.263	23.003			
100	1	53.143	40.394	1	38.857	29.536	1	66.634	50.649
	2	106.288	80.790	2	77.714	59.071	2	133.270	101.299
	3	159.434	121.186	3	116.570	88.606			
200	1	108.208	82.250	1	79.262	60.248	1	136.058	103.419
	2	216.417	164.500	2	158.522	120.495	2	272.117	206.839
	3	324.629	246.752	3	237.780	180.741			

5.3.2. Benchmark

Even after the bias correction, the error between $\mathbf{p}_{c,e}$ and $\mathbf{p}_{c,t}$ remains quite large for the EXP2 dataset. The NUM1 dataset also still has quite a large error for the higher orbits. If the error in real life is reverted to the scale of the experiment, a 3 km error is equal to 3 cm. This is still quite significant, since an error that large would reduce the usefulness of such an experimental set-up if that is the limit for accuracy in the set-up. To further investigate the source of the errors, a benchmark measurement was completed to find how accurate the manual point selection was when identifying the coordinates for each $\mathbf{r}_N$ in the image.

To determine the user error, the same three points were clicked ten times to see how accurately an individual point can be clicked and how large the difference is in each click because the user is unable to select the exact same point. It was found that for manual point selection the standard deviation was $\sigma = 1.21$ pixels. For EXP2 this would mean an error in the landmark positions in the image of $4.16 \cdot 10^{-3}$ mm and for NUM2 $3.14 \cdot 10^{-3}$ mm. To find the effect of these errors, a sensitivity analysis was performed.

5.3.3. Sensitivity analysis

Aside from the error in landmark positions, the sensitivity analysis can also be used to gain insight in how the position of the points in the image and uncertainties in the focal length influence the estimate. Table 5.4 shows the effect of an error e in the x coordinate, z coordinate and in both coordinates, on the error in $\mathbf{p}_{c,e}$. Here the error was applied to all landmarks used in the estimation. It becomes apparent that the error scales linearly. Furthermore, by applying the error to individual points, it was found that the error is directly proportionate to the magnitude of the coordinate. From Table 5.4 it can be found that while the human error in locating the landmarks is not negligible, it does not account for the large error still present in the EXP2 results. The human error appears to be a more significant portion of the $\mathbf{p}_{c,e}$ error in the NUM1 dataset. Additionally, as hypothesised in Subsection 5.3.1 the effect of the same error increases with increasing orbital radius.

The effect of the uncertainty in the focal length was also evaluated. Table 5.5 shows the average change in the estimation error due to a small change in the focal length. The focal length of EXP2_R_30 was found to be 8.56 mm during the camera calibration. However, as mentioned in Section 4.5, the focal length had to be adjusted during the experiment, making the exact focal length unknown. Since the focal length is used to determine the direction of the unit vectors used in calculating the position estimate (see Section 5.1), using the wrong focal length could have an effect on the accuracy of the estimate. By varying the focal length of EXP2 by 0.05 mm, the change in the position estimate is several times larger than the change due to human error in the landmark selection. The change in $x_{c,e}$ and $z_{c,e}$, due to the change in the focal length, was less than 10 m for all orbits and indices. Therefore the change in focal length can be assumed to only have an effect on $y_{c,e}$. This could also explain the large difference in the estimates for EXP2 and NUM1, since the NUM1 focal length is known with certainty. Additionally, it was found that this error also increases linearly. During the camera calibration the focal lengths found already varied by more than 0.1 mm, where the focus of the lens was not adjusted. The calibration could not be performed again to find the range of possible focal lengths and quantify the total uncertainty. However, from these results it can be assumed that part of the error in the position estimation can be accounted for by the uncertainty in the focal length.

Table 5.5: Change in camera position estimate error when a change is applied the focal length of the camera, both when increasing or decreasing the focal length

Orbit [km]	e_{fl} [mm]	$\Delta e_{\mathbf{p},c}$ [m]
30	0.05	120.337
100	0.05	554.555
200	0.05	1127.185

After these analyses it is apparent that the main source of the error in the EXP2 dataset compared to NUM1 is likely due to the execution of the experiment. Until the experiment has been recreated under more controlled conditions (automated camera positioning, fixed focal length with large depth of field, motion tracking and surface mapping), it is uncertain exactly how much can be contributed to the experimental set-up and how much to the inherent sensor measurement errors in the dataset.

5.4. Improvements for data processing

Since part of the error in the results can be attributed to uncertainties in the landmark position and human error (1% for EXP2 and around 10% for NUM1), the research could be extended by applying work previously research by Van der Heijden (2022) (see Chapter 1). Van der Heijden also made use of landmarks to estimate the “line-of-sight” distance from a camera to the subject. Where this study uses a simple OLS, his work used a convolutional neural network (CNN) to autonomously estimate the position of the camera. The trained CNN has an error of lower than 50 m, for an ideal camera (no skew or distortions), at orbital radii of less than 8 km. The median pixel error of the CNN of 1.9 pixels is similar to the pixel error found in this study. Thus the error will likely be similar in magnitude to the NUM1 dataset. However, the CNN does recognise outliers unlike the OLS. If there are inherent faults in the dataset due to the camera itself, the CNN would be able to detect these faults and correct the estimate accordingly. Van der Heijden mentions the necessity of testing the CNN with real images instead of numerically generated images, to bridge the gap between the simulated and the real performance. If the combination between the experimental images and the CNN can be made, the next step would be to include the distance estimate in a navigation filter.

Using the real navigation sensor measurements, such as the images created in this study, as input for a navigation filter can further extend the research into how robust the filter is. Taking a similar experimental set-up, where the asteroid is stationary and the sensor suite is moved around the asteroid using robotics. The navigation filter can be used to command the robotics in the simulated orbit, which will give a direct new input to the navigation filter using the new sensor measurements. Using an experimental set-up as such will allow for more methods of integrated systems testing before navigation filters have to unto hardware, potentially reducing the uncertainties in the performance of the navigation system.

5.5. Summary of findings

There were several causes to the error in the camera position estimate identified: the bias present in the dataset due to a misalignment between the optical axis and the centre of rotation of Eros, human error in the landmark identification and uncertainties in the experiment.

The bias was identified as the primary cause for the error in the x-coordinate $x_{c,e}$ of the camera position estimate $\mathbf{p}_{c,e}$ and its z-coordinate $z_{c,e}$. On average, the bias present in the dataset could account for more than 90% of the error in $x_{c,e}$ and $z_{c,e}$ for both the EXP and NUM datasets. However, the bias could account for less than 5% of the error in $y_{c,e}$ for the EXP2 dataset and less than 1% for the NUM1 dataset. The total error in $\mathbf{p}_{c,e}$ reduced by 15% and 25% on average for the EXP2 and NUM1 datasets respectively.

Next, a benchmark was established to determine the accuracy of the manual landmark identification. It was found that manual selection had a standard deviation of σ = 1.21 pixels. By performing a sensitivity analysis the effect of this deviation was quantified. At most, the human error could account for 1% of the total error for the EXP2 dataset, and 10% for the NUM1 dataset.

A second finding of the sensitivity analysis, was the effect of the focal length on the solution. During

the experiment the focal length had to be adjusted, which changed the focal length. The calibration of the camera had been done ahead of the experiment and the focal length after the adjustment is unknown. The calibration did give an insight into the likely range of the focal length, which was determined to be approximately 0.05 mm. Varying the focal length by 0.05 mm lead to a change in the error of $\mathbf{p}_{c,e}$ that was 10 times larger than the change due to human error. This effect is only observed in the EXP2 dataset, as the focal length of the NUM1 dataset is known. The uncertainty could be mitigated by using a camera and lens with a fixed focal length in future experiments.

Finally, the most likely source of the largest errors in EXP2 compared to NUM1 is the experiment. Since the exact position of the asteroid model and camera cannot be verified after the experiment has been completed, their relative positions cannot be confirmed. If the attitude of Eros at 0° rotation was different from initially assumed, the landmark locations used in the camera position estimate would be incorrect, leading to an incorrect estimate. Furthermore, the EXP2 and NUM1 could then not be compared one-to-one as the attitude of Eros between the two datasets would not be the identical. Suggested improvements would be to make use of a motion capture system to record all the relative positions in the experiment and to control all the components with robotics to increase the accuracy of the test set-up.

6

Conclusions and Recommendations

This chapter aims to answer the research questions posed in the introduction through the research done in this study. Section 6.1 will discuss the three sub-questions, after which the main research question will be evaluated. Finally, Section 6.2 will reflect on the research and make some recommendations to improve the work and for future research.

6.1. Conclusions

The first sub-question from for this study pertained the asteroid model in the experimental set-up and was stated as follows:

1. **How can a physical asteroid model be created, to accurately reflect the real asteroid in a scaled orbit simulation?**

The first consideration is the quality of the model of the asteroid. If the resolution of a 3D model is several orders of magnitude less than the considered surface resolution of the navigation camera, then a lot if information will be lost. Landmarks that are used for landmark tracking will be missing and artifacts of the model (such as vertices) will become visible in the images. In this study the model was made by Gaskell and had an average surface resolution of 27 m/pixel. The Hayabusa2 navigation camera that was used for reference had a 13.5 m surface resolution at the lowest considered altitude of 11.4 km.

Secondly, the method of manufacturing should have an accuracy capable of printing the model better than its own resolution. If the manufacturing method has a lower accuracy or resolution, the same holds as for the model itself. Landmarks and details will be lost during production and manufacturing artifacts will be visible on the surface of the asteroid. The surface of the asteroid holds the relevant information for relative navigation and should be recreated as accurately as the model allows. It was decided to use a stereolithography (SLA) printer, which cures layers of resin with UV to create the model. The printer has a resolution of 0.05 mm per layer which is two orders of magnitude smaller at the experiment scale of $10{:}1{\cdot}10^6$, than the resolution of the model. There were several challenges to the manufacturing. Consistent warping occurred in the printed model, causing the two halves of the asteroid to not fit together. Increasing washing and drying times, as well as removing the heat cycle during UV curing reduced the effect, but did not fully negate it. It was considered to print the asteroid model in one part, but the increased number of print supports attached to the surface of the asteroid would reduce quality of the model. As mentioned, the skin of the asteroid is most important for the images. This created an uncertainty in the model.

Lastly, to increase the realism of the images, a surface treatment was added. The resin from the SLA printer is reflective whereas an asteroid has a dusty surface. Using sand made the surface more matte, but was inappropriate for the small scale of the model. Matte spray paint was found as a solution, as the microscopic paint drops could be used to emulate a dusty surface. Having the right amount of light diffusion will make the shadows on the model more accurate. The final model used in the experiment still had brighter highlights, that might be reduced by building up the fine layers of paint more.

2. **How can an experimental set-up be created to most closely simulate in-orbit conditions?**

There are several points that need to be considered for the experiment set-up to increase the realism and accuracy; the lighting, the asteroid attitude and the camera position. For the lighting a lamp was used with three light-emitting diodes (LED's) that emitted a Sun-like spectrum. Using the three LEDs meant that the width of the light beam was too wide on the asteroid model. A singular light, preferably with more linear light, should be used to create more accurate lighting.

The attitude of the asteroid should be controlled. Here the asteroid was mounted on a tripod and placed on a rotating base, but after the experiment was completed there was no longer a record of the exact position or rotation the asteroid had been in. By having a stationary asteroid the uncertainty in rotation could be reduced. Creating a 3D scan of the set-up with a motion tracking system would fix the asteroid to a point in space which could be referred back to later for verification.

The same is true for the position of the camera. Using a laser range finder to position the camera was found to be insufficient in this experiment. By using preprogrammed robots, the position of the camera with respect to the asteroid could be set more accurately. Additionally, the 3D scan could also be beneficial for the camera, as the exact relative position of the camera and the asteroid could be recorded. By having a record of this, uncertainties in the evaluation of the results later in the analysis would reduce as well.

3. **How do experimental measurements compare to numerically simulated images for optical navigation simulations?**

To compare the experimental images to those that were numerically rendered, the position of the camera was based on the landmarks in the images. An error in the measurement would be reflected in the position estimate deviating from the numerical results. To estimate the camera position, an ordinary least squares was applied to find the intersection of the vectors between the landmarks and the camera. This method was not sensitive to outliers however, which made it hard to identify if a deviation in the estimate was due to faults in the image or in the execution of the experiment itself. The experimental images had a higher error in the position estimate, compared to the numerical images. There are several explanations for this; the position of the camera, manual landmark identification, uncertainties in the focal length, and uncertainties in the asteroid attitude.

As mentioned in the previous sub-question it is important to know exactly where the camera is in the experimental set-up. It was attempted to align the optical axis of the camera with the centre of rotation of the asteroid. However, when recreating the experimental images in the numerical dataset, it became apparent that this was done unsuccessfully. The offset of the optical axis from the camera to the y-axis (the intended alignment) had to be calculated and this bias correction was applied to the results. This improve the estimate of the camera position by a margin of 16%, but the large errors in estimate maintained for the experimental dataset.

Another possible source of error was the manual identification of the landmarks in the images. However, the manual selection was executed for both the experimental and the numerical dataset and thus does not explain the difference between the two. Additionally, the variation in location for each individual landmark only varied by 1.2 pixels, which was comparable to other studies, and the result of such an error was at most 1% for the experimental dataset. It did account for between 5-60% of the error in the numerical dataset.

Seemingly the largest source of the error that could be identified, was the focal length. A calibration was executed to determine the focal length. However, during the experiment the lens had to be refocussed, which changed the focal length to an unknown value. Varying the focal length by 0.05 mm, on a focal length of 8.56 mm, already created a change in the estimate of 10^2 m. This could be negated by using a lens with a fixed focal length and a large depth of field so the entire subject of the image is in focus regardless of the distance.

Lastly, since the exact attitude of the asteroid was not known after the experiment was concluded, the numerical dataset had to be recreated by eye. This could cause the landmarks that were used to estimate the camera position to have different relative positions in the experimental image. This too could lead to an error in the position estimate.

Taking these points into consideration, the main cause of difference between the experimental dataset and the numerical dataset was the set-up of the experiment. Numerical images are easier

to create as they do not require an experimental set-up, although they are limited in their realism. Using real sensors to capture these measurements means that real non-Gaussian errors are introduced in the measurement. It could give valuable insights into a navigation filter, to investigate how it handles unexpected errors.

How can experimental images be captured that can potentially be used to support the development of autonomous navigation systems for asteroid relative navigation?

To answer the main research question, the main points are the accuracy of the model and the experimental set-up. The model needs to have a high enough resolution that identifiable landmarks are visible on the optical navigation images. This includes the initial shape model, and the manufactured model. The manufacturing method influences the accuracy of the final product and should therefore be considered carefully. Evermore so, the influence that the experiment set-up has on the quality and therefore applicability of the experimental images. By creating a set-up with verifiable relative positions and reducing the uncertainties in the hardware used (such as the focal length) the performance of the navigation filter can be evaluated more accurately. If the initial errors are known well, then more can be said about the errors introduced by the navigation filter. Nonetheless, it would be interesting to see how a navigation system would perform with these images. A large cause of error seems to be uncertainties of the camera position with respect to the asteroid. If a navigation system would be able to find the correction in its position using pictures such as these it would make it very robust.

Numerical images could be used instead of the images created in an experiment. These do not require a full test set-up and have a lower cost to create. However, as mentioned at sub-question 3, it is the real errors in the dataset the could improve the analysis of a navigation system. In a real orbit there will be unexpected errors that the navigation system is required to deal with, as well as compounding errors. Van der Heijden (2022) suggests in his work that his methods for estimating the camera distance to the asteroid should be tested on experimental images instead of numerically rendered images. This work could be the first step to recreating his dataset experimentally. Furthermore, by recreating this experiment with a full sensor suite, the optical navigation imagery could be used as a direct input to the navigation filter together with the other sensors. In this manner system integration testing could be tested as well.

6.2. Recommendations

Based on this study, there are several recommendations that can be made. For the asteroid model, the method of manufacturing should be reconsidered. Either more research needs to be done on how to fully negate the warp in the model, or a method should be found that allows the construction of the model in one piece without reducing surface quality. Depending on the orbits that will be tested it may be possible to print an asteroid model in one piece with the supports on the eclipse side of the asteroid. This would only be possible if the asteroid has a dark side for an extended period of its orbit. The surface treatment with spray paint seemed relatively successful, although more layers of paint would be advised.

For the experiment, as mentioned in sub-question 2, using robotics to move the asteroid or the sensors would allow for more accurate positioning. The use of motion tracking could record all relative positions and orientations of the sensor and the asteroid during the measurement, to reduce uncertainties. Different lenses should also be used in any future experiment, to avoid a variable focal length. Furthermore, the orbit considered here was equatorial around Eros, which has a fully eclipsed side for part of its orbit around the Sun. Therefore, the dataset does not contain images of a more than 80% eclipsed Eros. It would be interesting to have a full dataset of an orbit around an asteroid that includes an eclipse, to be able to test the robustness of the time propagation in a navigation system. To accomplish this, a different asteroid could be used, which is possible as long as a shape model exists with a high enough resolution. Also, the Sun-like light would have to be moved accordingly with the orbit, and positioned as such that it does not interfere with the sensors by having the sensors cast an unrealistically large shadow on the surface of the asteroid.

Additionally, a mapping phase could be added to the experiment. Since the landmarks were selected after the experiment, the exact positions in the inertial frame might be incorrect. By mapping the landmarks as part of the experiment, the landmarks can be expressed in an asteroid reference frame, increasing the realism of the analysis.

Lastly, for the analysis of the quality of the dataset, a different least squares solution should be used. The position estimate was calculated using an ordinary least squares (OLS) to solve a linear system, but an OLS is not sensitive to outliers. Therefore any individual error in landmark identification could lead to a large error in the estimated position. Different methods of estimating the camera position could also be considered, such as the convolutional neural network developed by Van der Heijden. Furthermore, the linear system of equations itself could be improved upon. To estimate the camera position the assumption of a pin hole camera was made. This has some limitations and it would be beneficial to see the effect of this assumption.

Bibliography

Antreasian, P. G., Adam, C. D., Berry, K. E., Geeraert, J. L., Getzandanner, K. M., Highsmith, D. E., Leonard, J. M., Lessac-Chenen, E., Levine, A., McAdams, J. V., McCarthy, L. K., Moreau, M. C., Nelson, D. S., Page, B. R., Pelgrift, J. Y., Rieger, S., Sahr, E. M., Wibben, D. R., Williams, B., … Lauretta, D. S. (2022, February). Comparing Pre-Launch Assumptions to In-Glight Navigation Performance fo OSIRIS-REx. In: 44th Annual AAS Guidance and Control Conference. (AAS 22-167). American Astronautical Society. Breckenbridge, Colorado, 2022.

Bedshore, E., Sutter, B., Mink, R., Lauretta, D., Moreau, M., Boynton, W., Dworkin, J., Shinohara, C., Everett, D., & Gal-Edd, J. (2015). The OSIRIS-REx Asteroid Sample Return Mission. In: IEEE Aerospace Conference. IEEE. Big Sky, MT, 2015. https://doi.org/10.1109/AERO.2015.7118989

Berry, K., Sutter, B., May, A., Williams, K., Barbee, B. W., Beckman, M., & Williams, B. (2015). OSIRIS-REx Touch-And-Go (TAG) Mission Design and Analysis. In: 36th Annual AAS Guidance and Control Conference. American Astronautical Society. Breckenridge, CO, 2015, February.

Blobel, V. (2005). Linear least squares. *Lecture slides, University of Hamburg*. https://www.desy.de/~sschmitt/blobel/blobel_leastsq.pdf

Bourgeaux, A. (2020). *Autonomous estimation of the gravity field for asteroid missions* [Master's thesis, University of Bologna].

Chanut, T. G. G., Winter, O. C., & Tsuchida, M. (2014). 3D stability orbits close to 433 Eros using an effective polyhedral model method. *Monthly Notices of the Royal Astronomical Society*, *438*, 2672–2682. https://doi.org/10.1093/mnras/stt2383

Cheng, A. F. (2002). Near Earth Asteroid Rendezvous: Mission Summary. In *Asteroids III* (pp. 351–366). University of Arizona Press.

Cheng, A. F., Santo, A. G., Heeres, K. J., Landshof, J. A., Farquhar, R. W., Gold, R. E., & Lee, S. C. (1997). Near-Earth Asteroid Rendezvous: Mission overview. *Journal of Geophysical Research*, *102*(10), 695–708. https://doi.org/10.1029/96JE03364

Dombard, A. J., Barnouin, O. S., Prockter, L. M., & Thomas, P. C. (2010). Boulders and ponds on the Asteroid 433 Eros. *Icarus*, *210*, 713–721. https://doi.org/10.1016/j.icarus.2010.07.006

Dubois-Matra, O., Casasco, M., Sanchez Gestido, M., & Huertas Garcia, I. (2024). ESA Technology Developments in Vision-Based Navigation. In: In *Proceedings of the IUTAM Symposium on Optimal Guidance and Control for Autonomous Systems 2023*. IUTAM Bookseries, vol. 40. Springer, Cham, 2024. https://doi.org/10.1007/978-3-031-39303-7_3

Farquhar, R., Kawaguchi, J., Russell, C., Schwehm, G., Veverka, J., & Yeomans, D. (2002). Spacecraft Exploration of Asteroids: The 2001 Perspective. *Asteroids III*.

Foucher, F., Hickman-Lewis, K., Hutzler, A., Joy, K. H., Folco, L., Bridges, J. C., Wozniakiewicz, P., Martínez-Frías, J., Debaille, V., Zolensky, M., Yano, H., Bost, N., Ferrière, L., Lee, M., Michalski, J., Schroeven-Deceuninck, H., Kminek, G., Viso, M., Russell, S., … Westall, F. (2021). Definition and use of functional analogues in planetary exploration. *Planetary and Space Science*, *197*. https://doi.org/10.1016/j.pss.2021.105162

Gaskell, R. W. (2004, May 17-21). High Resolution Shape Topography of Eros - Preliminary Results From NEAR Imaging Data. In: 2004 Joint Assembly. JPL. Montreal, PQ, Canada, 2004.

Gaskell, R. W. (2008). Gaskell Eros Shape Model V1.0 NEAR-A-MSI-5-EROSSHAPE-V1.0 NASA Planetary Data System [Retrieved on 16-05-2023 from https://3d-asteroids.space/asteroids/433-Eros].

Han, D., Kennedy, B., Rush, B., Grebow, D., Mastrodemos, N., Whiffen, G., Bradley, N., & Karimi, R. (2019, March). Dawn's Final Mission at Ceres: Navigation and Mission Design Experience. In: 18th Australian Aerospace Congress. Melbourne, 2019.

Kaasalainen, S., Kaasalainen, M., & Piironen, J. (2005). Ground reference for space remote sensing. *Astronomy & Astrophysics*, *440*, 1177–1182. https://doi.org/10.1051/0004-6361:20053199

Lauretta, D. S., Balram-Knutson, S. S., Bedshore, E., Boynton, W. V., Drouet d'Aubigny, C., DellaGiustina, D. N., Enos, H. L., Golish, D. R., Hergenrother, C. W., Howell, E. S., Bennett, C. A., Morton, E. T., Nolan, M. C., Rizk, B., Roper, H. L., Bertels, A. E., Bos, B. J., Dworkin, J. P., Highsmith, D. E., … Sandford, S. A. (2017). OSIRIS-REs: Sample Return from Asteroid (101955) Bennu. *Space Science Reviews*, *212*, 925–984. https://doi.org/10.1007/s11214-017-0405-1

Leica Geosystems. (2020). *Leica DISTO X3: The original laser distance meter*. Leica Geosystems. https://shop.leica-geosystems.com/sites/default/files/2020-01/Leica%5C_DistoX3%5C_UM%5C_nl.pdf?srsltid=AfmBOor5Rq4WPGJya3UrrlkCiNLNOtajKkIVcyeAruaOVGpVCQu5mtlq

Lissauer, J. J., & De Pater, I. (2013). *Fundamental planetary science: Physics, chemistry, and habitability*. Cambridge University Press.

Lorenz, D. A., Olds, R., May, A., Mario, C., Perry, M. E., Palmer, E. E., & Daly, M. (2017, March). Lessons Learned from OSIRIS-REx Autonomous Navigation Using Natural Feature Tracking. In: 2017 IEEE Aerospace Conference. IEEE, 2017, 1–12. https://doi.org/10.1109/AERO.2017.7943684

Michikami, T., & Hagermann, A. (2021). Boulder sizes and shapes on asteroids: A comparative study of Eros, Itokawa and Ryugu. *Icarus*, *357*. https://doi.org/10.1016/j.icarus.2020.114282

Mooij, E., & Root, B. C. (2024, January 08-12). Gravity-Field Estimation of Asteroids. In: In *Proceedings of the AIAA SCITECH 2024 Forum*. Article AIAA 2024-2275 (AIAA SciTech Forum and Exposition, 2024). American Institute of Aeronautics and Astronautics Inc. (AIAA), 2024. https://doi.org/10.2514/6.2024-2275

Muñoz, P., Budnik, F., Godard, B., Morley, T., Companys, V., Herfort, U., & Casas, C. (2012). Preparations and strategy for navigation during Rosetta comet phase. In: 23rd International Symposium on Space Flight Dynamics. Pasadena, USA: ISSFD, 2012.

Munuera Vilalta, M. (2024). *Asteroid Gravity Field Estimation by a Satellite Constellation* [Master's thesis, Delft University of Technology].

Norrdine, A. (2012, November 13-15). An Algebraic Solution to the Multilateration Problem. In: 2012 International Conference on Indoor Positioning and Indoor Navigation. 2012. https://doi.org/10.13140/RG.2.1.1681.3602

Norrdine, A. (2018). Trilateration Matlab code. Paper: An Algebraic Solution to the Multilateration Problem. [Retrieved on 13-09-2024 from https://www.researchgate.net/publication/288825016_Trilateration_Matlab_Code%20Index].

Oshima, T., Terui, F., & Tsuda, Y. (2022, January). 3 - Spacecraft system design of Hayabusa2. In M. Hirabayashi & Y. Tsuda (Eds.), *Hayabusa2 Asteroid Sample Return Mission* (pp. 25–48). Elsevier. https://doi.org/10.1016/B978-0-323-99731-7.00003-9

Razgus, B. (2016). *Relative Navigation in Asteroid Missions: Dual Quaternion Approach* [Master's thesis, Delft University of Technology].

Formlabs. (2021, December). *Manual - Form 3L: Large-format Low Force Stereolithography (LFS) 3D printer - Installation and Usage Instructions*. Formlabs. https://media.formlabs.com/m/5f0ed4f707037528/original/-ENUS-Form-3L-Manual.pdf

Russel, C. T., Raymond, C. A., Fraschetti, T. C., Rayman, M. D., Polanskey, C. A., Schimmels, K. A., & Joy, S. P. (2005). Dawn mission and operations. In D. Lazzaro, S. Ferraz-Mello, & J. Fernández (Eds.), *Asteroids, comets, meteors*. Proceedings IAU Symposium. https://doi.org/10.1017/S1743921305006691

Sorsa, L. I., Eyraud, C., Hérique, A., Takala, M., Pursiainen, S., & Geffrin, J. M. (2021). Complex-structured 3d-printed wireframes as asteroid analogues for topographic microwave radar measurements. *Materials and Design*, *198*. https://doi.org/10.1016/j.matdes.2020.109364

Spee, S. J. H. (2022). *Asteroid gravity field estimation below the Brillouin sphere* [Master's thesis, Delft University of Technology].

Suzuki, H., Yamada, M., Kouyama, T., Tatsumi, E., Kameda, S., Honda, R., Sawada, H., Ogawa, N., Morota, T., Honda, C., Sakatani, N., Hayakawa, M., Yokota, Y., Yamamoto, Y., & Sugita, S. (2017). Initial inflight calibration for Hayabusa2 optical navigation camera (ONC) for science observations of asteroid Ryugu. *Icarus*, *300*, 241–359. https://doi.org/10.1016/j.icarus.2017.09.011

Thomas, P. C., Joseph, J., Carcich, B., Clark, B. E., & Veverka, J. (2000). The Shape of Eros from NEAR Imaging Data. *Icarus*, *145*, 348–350. https://doi.org/10.1006/icar.2000.6406

Tsuda, Y., Takeuchi, H., Ogawa, N., Ono, G., Kikuchi, S., Oki, Y., Ishiguro, M., Kuroda, D., Urakawa, S., Okumura, S., & Hayabusa2 Project Team. (2020). Rendezvous to asteroid with highly un-

certain ephemeris: Hayabusa2's Ryugu-approach operation result. *Astrodynamics*, *4*(2), 137–147. https://doi.org/10.1007/s42064-020-0074-9

Van der Heijden, L. F. J. (2022). *Autonomous Navigation around Asteroids using Convelutional Neural Networks* [Master's thesis, Delft University of Technology].

Van Oorschot, M. N. (2022). *Sensor Fusion in Autonomous Navigation for Asteroid Observation Missions* [Master's thesis, Delft University of Technology].

Watanabe, S., Tsuda, Y., Yoshikawa, M., Tanaka, S., Saiki, T., & Nakazawa, S. (2017). Hayabusa2 Mission Overview. *Space Science Reviews*, *208*, 3–16. https://doi.org/10.1007/s11214-017-0377-1

Zwick, M., Huertas, I., Gerdes, L., & Ortega, G. (2018). *ORGL - ESA's Test Facility for Approach and Contact Operations in Orbital and Planetary Environments* (tech. rep.). European Space Agency.

A

3D Printing Documentation

Section A.1 contains the documentation that was created based on the lessons learnt creating the physical asteroid model in the SLA printer. The full process of creating the 3D model is given first, followed by additional comments on several of the steps. Section A.2 contains an overview of the design iterations of the physical asteroid model.

A.1. Tips and tricks for 3D printing

Checklist 3D printing with SLA printers

1. Create/adapt model in Fusion360/Meshmixer
2. Upload part to Preform.
3. Check orientation, add supports, check if there are no cups.
4. Check whether there is enough resin in the cartridges.
5. Check if the print plate is clean.
6. Start the print.
7. Check if the print was in fact successful.
8. Remove print plate and model from printer and close printer door.
9. Get IPA from storage.
10. Fill washer with siphon.
11. If model can be washed on print plate:
    a. Move print plate to washer and start the wash.
    b. After washing, remove the print from the print plate and gently clean off any excess cured or liquid resin still on the plate with a knife and IPA.
    c. Put the print plate back in the printer.

    If model has to be removed from print plate:
    a. Remove model from print plate (try to keep the supports intact)
    b. Move model to washer and start the wash.
    c. While the model is washing, clean the print plate and gently clean off any excess cured or liquid resin still on the plate with a knife and IPA and put it back in the printer.
12. Put model on a paper towel under the fume vacuum and leave to dry until COMPLETELY dry (I'd suggest at least a day for larger prints)
13. Empty the washer with the siphon.
14. Put IPA back in storage.
15. When the model is completely dried
    a. Remove supports and then put it in the curer for 3x the suggested curing time for the resin you printed in and disable the (pre)heating cycle.

    OR
    b. Put it in the curer for 3x the suggested curing time for the resin you printed in and disable the (pre)heating cycle and then remove supports.

Tips and tricks printing (sorted by step of the checklist)

1 Fusion360 or Meshmixer

- Fusion360 if you're building the model.
- Meshmixer if you're adapting a model (very computationally heavy. Used in this study)

Meshmixer:

- Theres some good online tutorials (YouTube mainly) on how to create hollow models with infill etc.
- Be careful using the Combine function. It is the fastest and most accurate way to attach 2 pieces in Meshmixer, but the model maintains 2 separate meshes that are "glued" together. When trying to load the model into the printer software, the parts where the meshes overlap (so the internal overlap) are removed. So you lose all your attachment points.
- If you use combine, make sure to use make solid after. This remakes the mesh into 1 large part.
- Use Booleans where you can, but be careful with your Boolean settings, because you might lose some detail in the model if Booleans are not used correctly.
- Make solid can also be used after Boolean operations, it is advisable to use make solid at least once, before you try to print the model to make sure the mesh is printable. Again, be mindful of the settings, since make solid "remakes" the mesh to one whole, so some details might get lost if the settings are suboptimal.

Design specifications to consider when creating the model[1]

3 For the printer we use (Formlabs 3L), you need to upload your model to their software called Preform to send it to the printer. There are several things to look out for:

- The orientation of the part in the printer has a large influence on the quality and performance of the print. If there are large horizontal surfaces that you need to print, either print on the bed itself (though the first few layers have a longer laser cure time to make sure that the print adheres to the print plate properly. These layers might look different so if you can, I would suggest propping the model up on supports. If you add supports this is defaulted in Preform).
  If you have a large surface parallel to the print plate, but on print supports, that the surface will not be able to print perfectly flat due to the overhangs between the print supports. It is advisable to print at at least 45 degrees from the print plate, as at this angle there are no supports necessary for the overhang. Less supports means less surface artifacts, and less post processing. Any larger angle up to 90 degrees works just as well, depending on the rest of your model (note, circular holes don't print round when they are perpendicular to the print plate due to the overhang at the top. There are tutorials online on how to deal with this).
- As mentioned before, orientation is also important to consider when adding supports. The number of supports might be limited depending on the orientation, and if there are parts of the model that need to press fit, or have very tight allowances, it is best to limit the number of supports there. There is the option to manually add and remove supports in Preform if the autogenerated ones do not cut it.
- The last point on orientation is to watch out for "cupping"[2]. Preform does check for cupping when it is performing its health checks, so make sure to always complete the health check before printing. Cupping occurs when there is a pocket in the model, which can be fully closed by the tank when the new layer is cured on. There needs to be a way for the air to get back in when the print plate moves away from the tank, or a vacuum can occur and pull the model apart.
- There is the option to either use a full "raft" to which print supports are attached, which in turn is stuck to the print plate, or to use mini "rafts". Mini rafts use less resin compared to full rafts and are easier to remove from the print plate. However, mini rafts are more prone to coming off the print plate, causing print failure. This is only likely to occur with large prints, and the Preform software will give you a warning if that is the case. You need to decide before hand if you wish to wash your print on the print plate or remove it from the print plate

[1] https://support.formlabs.com/s/article/Design-specifications-for-3D-models-form-3?language=en_US [Cited: 15-08-2024]
[2] https://support.formlabs.com/s/article/Cupping-Blowout?language=en_US [Cited: 15-08-2024]

before washing (more on that later), as I've been keeping the support structures attached when washing the print separately and that is only possible with a full raft. Mini rafts are easier to remove, but much harder to keep intact and attached to the model.

4 Step 1 when you want to print your first print is to get in touch with the lab technician responsible of the printer. Follow the safety instructions well, as the resin you'll be working with is harmful to the skin in its liquid form, and when it is dissolved in Isopropyl alcohol (IPA) it is very hazardous.

- Before printing the part, check whether there is enough resin in the tanks on the printer. If you have access to the online dashboard, you'll get a notification that one of the cartridges is empty, but you might not be able to access the printer to replace a cartridge. You can also find the resin levels on the printer itself.
- When inserting the new cartridge be sure to move it around a bit to mix the pigment and the resin. If there is some time between prints it might be a smart idea to take the cartridge from the printer to mix the resin again, before putting it back for printing. You'll see it in the printer as well. The pigment might separate from the resin if it sits in the printer tank for a while. You do not have to manually mix this. The printer will mix the resin in the tank before printing. It is important that you avoid touching the bottom of the tank at all cost, since any scratches on the film at the bottom of the tank can cause the laser to disperse, and the print quality to go down.
- If you have to prep a new resin tank for the printer, empty one full cartridge of resin into the tank when it is installed. Otherwise, it will start filling the tank from the cartridges on the side, and this will take very long and will largely empty them. By emptying a cartridge, the process is much faster.

5 Before starting a print, check whether the print plate is fully cleaned by taking it out of the printer and using the light. The scratches on the plate make it harder to see at first glance whether there is still some cured resin on the plate.

10 The washer opens from the top. The jerry cans are too large to lift and dump the contents into the large washing basin. The front of the washer has a door, where below the IPA tank there is some space to store an electric siphoning pump.
Put the large grey "stick" into the liquid you wish to transfer and clip the black end to the sides of the IPA tank in the washer. There are lines on the inside of the tank which indicate how full the tank must be when you are planning on washing the model while it is still attached to the plate. There is also a sensor located at the tip of the black end of the pump. When the IPA levels reach the end of the pump, the pump will start beeping to alert you that the tank is full and it will shut off. Double check if the IPA is up to the line if you need it to be there, since some of the liquid will drain back out trough the pump when it stops pumping. If you are going to wash a larger model, you can leave some of the IPA out, because otherwise the tank might overflow.

11 Depending on the geometry of your print you can either wash it while still on the print plate, or you might have to remove the part before washing. If the model has a pocket that will "catch" the IPA it will be hard to get it out of the washer without spilling the IPA everywhere. Otherwise, it is easiest to wash it on the plate, as removing the model from the print plate is easier without the excess resin on the plate making it slippery and sticky.
When you are removing the model from the print plate before washing, I've been keeping the supports intact and attached to the model until after curing, to avoid warping any edges. The main cause of warpage is the drying time and curing temperature (see steps 12 and 15), so removing the supports at this stage is likely not a problem, but keep it in mind.

12 When the washer has finished carefully drain any IPA that might be caught in the model in the tank when removing your model. If there is a hollow pocket in your model that you can fill with IPA, it is advisable to rinse that pocket out manually a few times as the washer might have a hard time agitating the IPA in there. Put down some paper towel and put your model on the towel under the fume vacuum. Leave the model there until it is *completely dry*[3]. The cured plastic might have absorbed some IPA and if you cure it too soon, some of the absorbed IPA will expand as it turns to vapor which could warp your model. Note that the lowest point of your model will be the last to dry, so do check the entire model to see if it dry. Side note: when the model is fully dried some of the resins are already safe to handle. White V4 resin is safe after being cured in the printer, but

[3]https://forum.formlabs.com/t/excessive-part-warpage-during-curing/35670/5 [Cited: 15-08-2024]

it needs to be cured to improve the strength of the model. Other resins are not safe to touch until after they have been cured. Consult the Formlabs documentation for the resin you are using.

13 While the model is drying, the washer can be emptied. Since the washer for the From 3L is so large, the IPA cannot be left in the washer due to safety regulations, since it is not used regularly enough. Therefore, if the washer is not used again that day, the IPA needs to be put back into its containers. This process is the same as step 10, but the pump is turned around (clipping the black end to the jerry cans instead of the washer tank).

15 When the model is curing it is important to disable the heating cycles in the curer. According to the Formlabs documentation[4] by heating the plastic it can cure faster to its optimal strength. However, several users[5] have reported that their models warp in the curer with the heating cycle. Therefore, both the preheat, and the heating during the curing cycle should be disabled for the best result. To still get to the high strength performance, it is advised to cure the model for 3 times the suggested length when the heating cycle is disabled. For example, White V4 should cure for 30 minutes at 60 degrees Celsius according to the default settings. In this case it would be cured at room temperature for 90 minutes.
Whether you remove the supports before or after curing is a preference. The supports are softer when the model is not yet cured, and some blemishes might still be evened out with IPA. However, there is a risk of warping the model as the polymers are not fully set yet.

A.2. Prototyping documentation

Table A.1 shows the dimensions of all the design iterations and printing prototypes for the 3D model of Eros. Prototypes were first built in Meshmixer and then exported to PreForm to see if there were any printing conflicts in the design. Some of the attempted dimensions are excluded due to the model becoming too complex for the simulation to compute.

[4] https://formlabs-media.formlabs.com/filer_public/ac/89/ac8963db-f54a-4cac-8fe9-fb740a7b06f1/formlabs-materials-library.pdf [Cited: 15-08-2024]

[5] https://forum.formlabs.com/t/excessive-part-warpage-during-curing/35670/6 [Cited: 15-08-2024]

Table A.1: All design iterations of the 3D model of 433 Eros. Skin thickness t, infill thickness t and infill spacing s are given for each scale model, along with the dimensions of the alignment pins, at which date it may have been printed, and any further changes or observations made to the models.

Iteration	Name	Scale	Skin t [mm]	Infill t [mm]	Infill s [mm]	Pin [mm]	Pocket [mm]	Printed [dd/mm/yy]	Note
1	Eros15_1	15:1e6	2	4	30	5x5x6	5x5x6.2		Infill was rotated by 45 degrees around 2 axis, required a lot of support material
2	Eros15_2	15:1e6	2	4	30	5x5x6	5x5x6.2		Infill was rotated by 45 degrees around 3 axis
3	Eros7,5_1	7.5:1e6	1	2	15	5x5x6	5.4x5.4x6.4	13/09/'23	1 mm skin is too thin, full raft supports, more infill to reduce print supports, increased tolerance on depth pocket. Remove model from print plate before washing
4	Eros15_3	15:1e6	2.5	3	20	5x5x6	5.4x5.4x6.4		Still needs internal supports. Higher density infill does not compute
5	Eros15_4	15:1e6	3	5	20	5x5x6	5.4x5.4x6.4		For thicker skin, higher density infill still does not compute
6	Eros15_5	15:1e6	3	5	25	5x5x6	5.4x5.4x6.4		Needs some more supports when printing, but largely supports itself internally
7	Eros20_1	20:1e6	3	5	25	5x5x6	5.4x5.4x6.4		Needs significant amount of internal print supports
8	Eros15_3_2	15:1e6	2.5	3	20	5x5x6	5.4x5.4x6.4		Same as Eros15_3, but infill is rotated to attempt 45 degrees on all infill pins at printing orientation, so that no supports are required on the infill when printing
9	Eros15_6	15:1e6	2.5	7	30	5x5x6	5.4x5.4x6.4		
10	Eros15_7	15:1e6	2.5	6	30	5x5x6	5.3x5.3x6.4	25/09/'23	Best option at this scale for least amount of resin. Printable without internal print supports, save 1 at the top skin. Printed with mini rafts, severe warping present.
11	Eros15_7_2	15:1e7	3	6	30	5x5x6	5.3x5.3x6.4		
12	Eros20_2	20:1e6	2.5	6	30	5x5x6	5.3x5.3x6.4		To fit printer, this model has to be cut into quarters instead of halves
13	Eros7,5_2	7.5:1e6	2	5	30	5x5x6	5.3x5.3x6.4	01/11/'23	Using full raft print supports and printed with the cut line between the halves vertically oriented to ensure a straight edge. Still some warping, seemed to warp during cure cycle. Vertical orientation did improve quality but more supports on the skin and thus more post processing. Next time use sheet to stabilize the openings
14	Eros7,5_3	7.5:1e6	2.5	5	30	5x5x6	5.3x5.3x6.4		
15	Eros7,5_4	7.5:1e6	2.5	5	30	5x5x6	5.3x5.3	01/11/'23	Pockets cut through the stringer sheet, added holes to sheets for IPA wash. Less warping and let dry completely without removing print supports. Some warping still present along 1 part of the edges. Added 2 mm thick stringer sheet, with 3x3x1 mm L-stringer at 15 mm spacing
16	Eros10_1	10:1e6	2.5	5	30	5x5x6	5.3x5.3		Extra thickness at the z-axis to allow a hole to be drilled for an M3 threaded insert
17	Eros10_2	10:1e6	2.5	5	30	5x5x6	5.3x5.3		Instead of added thickness, a cylinder is added for the insert to be put into. The hole in the skin will be pre-made and the cylinder high enough to glue to insert in firmly
18	Eros10_3	10:1e6	2.5	5	30	3x3x11	3.4x3.4	01/12/'23	Changed L-stringer spacing to 20 mm. Printed whole, delamination occurred due to faults in the printer. Likely damage to the bottom of the tank or dirty optics
18.2	Eros10_3	10:1e6	2.5	5	30	3x3x11	3.4x3.4	25/01/'24	Printed in two halves after optics were cleaned. Large warps still present, likely due to printer faults.
18.3	Eros10_3	10:1e6	2.5	5	30	3x3x11	3.4x3.4	20/02/'24	Left half only was printed to see if printed was fixed after replacing the resin tank and running diagnostics. Left to dry for 4 days, last day orientation was changed to allow any last vapours to escape the part. 1.5h cure without preheat or heating cycle
18.4	Eros10_3	10:1e6	2.5	5	30	3x3x11	3.4x3.4	23/02/'24	Right half was printed following the same steps as the left half. Some gaps still exist along the edge where the two halves meet. Unlikely a solution can be found in the given time frame and the gap is small enough that it can likely be fixed during post processing.

B

Experiment Documentation

The complete experiment plan is given in Section B.1, followed by the Blender settings in Section B.2.

B.1. Experiment plan

Supplies

- 1x tripod
- 1x mic-stand
- 1x lazy Susan
- 1x MDF plate (94,5 cm x 60,7 cm)
- 1x angle ring (ring that can be mounted on the MDF plate that shows a full 360 degrees)
- 1x degree indicator
- 1x Camera
- 1x mounting plate to attach camera to mic-stand
- 1x Laser range finder for calibration
- 1x Calibration square
- 1x Asteroid model
- 1x Threaded bar
- 1x “Sun” lamp
- 1x Computer
- 1x Power supply

Steps preparation

1. Install sensor drivers
2. Check if sensors functional
3. Perform calibration measurements for camera with calibration square
4. Perform calibration measurements with LRF by measuring predetermined distance
5. Verify angle measurement accuracy

Tuning aperture camera lens

1. Set the aperture as wide as possible (smallest f-stop value)
2. Set camera at a distance similar to the measurements
3. Use a book with an X marked in the middle and stand it up, and a ruler inclined at around 30 degrees (leaning against a mug for example). Make sure that the center point of the ruler is level with the X on the book.
4. Focus the lens on the x and the middle of the ruler.
5. See how much blurriness you can see at the bottom of the ruler (in the front of the image) and the top of the rules (the back of the image)
6. Find an aperture that reduces the depth of field, while still keeping the image in focus

Calibration camera

1. Print calibration square (including white border, and at a size that the entire calibration square can be seen in the image)
2. Put calibration square on a hard surface
3. Measure the size of the squares
4. Mount camera on the mic-stand
5. Position camera calibration squares under the lamp
6. Position camera at distance to the squares that is equal to the orbital radius of the experiment
7. Ensure that the entire calibration square is visible in the image
8. Capture images of the calibration squares at varying angles (smaller than 45 degrees) over the entire field of view of the camera (more than 10 images)
9. Input the images into the MATLAB Single Camera Calibrator App
10. Repeat at both 30 cm and 2 m distance, both at full and at half light

Verification rotation angle

1. Mount the laser range finder on the tripod that is positioned in the center of the MDF plate
2. Position a plate at the other end of the room, so that the laser can reach the plate
3. Turn on the laser by starting a measurement and mark the position of the laser on the plate
4. Measure the distance to the plate with the laser 3x and note the measurements
5. Rotate the MDF plate by a set angle
6. Turn on the laser by starting a measurement and mark the position of the laser on the plate
7. Measure the distance to the plate with the laser 3x and note the measurements
8. Measure the distance between the two points on the plate
9. Using the law of cosines, determine the angle that the laser rotated and determine the error compared to the expected rotation
10. Repeat 5 times for one angle, and for different angles, at different points on the ring on the MDF plate (6 degrees L – L, incomplete half degree indicator (v) – L, complete half degree indicator (◊) – L, R – L, crossing a gap L – L)

Verification camera position

1. Mount the camera on the attachment piece to the mic-stand
2. Add the laser range finder to the bottom of the attachment piece with the ¼” thread
3. Calculate the difference in position of the laser to the focal point of the camera
4. Use the laser range finder to set the distance of the camera to the center of the asteroid (from the focal point to the center of the ¼” rod)
5. Measure the distance between the camera and the center of the asteroid 5 times, and note the measurements.
6. Use the average to determine if the distance is correct
7. Check the camera is aligned by aligning the camera with the laser to the ¼” rod of the asteroid

Verify inertial attitudes asteroid and camera

1. Use the periscope in the geodetic tripod to verify that the asteroid is positioned right above the center of rotation
2. Tie a mass to a string and level the rod on which the asteroid is mounted with the sting (perfect vertical)
3. Position the calibration squares behind the camera and the asteroid
4. Check if the attitude of the camera matches the attitude of the asteroid, so they align inertially.
5. Repeat along other 2 axis

Steps experiment

1. Add threaded bar to tripod
2. Mount asteroid bar to the threaded bar on the tripod
3. Put the tripod on the MDF plate on the lazy Suzan, and position the 3 legs to be in 3 of the designated circles at equal distance to each other
4. Hang “Sun” lamp from the trusses and hook up power supply
5. Set desired ampere limit
6. Tack the indicator flag to the floor next to the ring
7. Mount the camera on the mounting plate
8. Add the mounting plate to the mic-stand
9. Add the LRF to the mounting plate
10. Connect camera to computer and secure the wiring
11. Set-up computer behind the camera so the light doesn’t interfere
12. Verify that the camera and LRF are working
13. Perform verification of position asteroid and tripod
14. Perform camera position verification
15. Remove the LRF from the mount
16. Set image name to name of the experiment (make sure to restart Galaxy to reset the count) EXPn_R_##_index.png for example: EXP1_R_30_1.png, EXP1_R_30_2.png…. where EXP1 indicates it is the first experiment for this set-up, R is radius, 30 is the simulated 30km radius, and the index indicates which measurement it is. Store rotation angle for each index in Excel and on paper. EXP1 is with full light EXP2 is with half light (limited at 1.1A)
17. Turn on Sun lamp (set timer for 6 minutes for EXP1 as a reminder to turn off the lamp and let it cool for 3 minutes so it doesn’t overheat. For EXP2 the lamp does not overheat)
18. Take images of test set-up for documentation
19. Check if the indicator flag is in the correct position (at 0 degrees for the first measurement)
20. Turn off headlamp
21. Set white balance once in Galaxy and determine and note the shutter speed
22. Capture image in Galaxy
23. Verify that the image was captured at the correct index
24. Mark the measurement as successful in the Excel and make any notes if necessary
25. Turn on headlamp
26. Get on your knees next to the indicator flag and put you dominant eye in line with the “flag pole”
27. Close your non-dominant eye and rotate the base 2 degrees, making sure that the right side of the flag is level with the degree line of the ring
28. Turn off headlamp
29. Repeat steps 22-28 until one full rotation has been made at 181 measurements (taking a break when the timer for the lamp goes off)
30. Keep note of any discrepancies both in the Excel and on paper
31. Update experiment plan to reflect challenges that occurred during set-up and execution
32. Verify that all images are stored and that index on noted corresponds to index reached with the images.
33. Put images in designated folders and make backup on drive
34. Deactivate camera and add lens cap. Remove camera from bracket and mic stand, and put bracket with camera in storage.
35. Put mic stand in storage
36. Dismount the asteroid and store carefully, to not damage the surface finish
37. Remove threaded bar from tripod and store with asteroid.
38. Return tripod to Bart, by first removing orange top and returning it to its case and then collapsing the tripod.
39. Store the rotating base
40. Disconnect all the wires from the lamp and power supply, put wires back in storage.
41. Remove zip ties (don’t cut! They open) from power supply and give it back to Joshua
42. Remove lamp from ceiling by lifting and turning and give back to Joshua
43. Document.

B.2. Blender settings numerical dataset

These are the settings used in Blender to render the images used in the NUM datasets. Figure B.1 shows the settings used for the shading. These settings recreate the light as it would be in space, with the elevation set to 90 degrees to put the Sun in the correct position to Eros, with respect to how Eros is rotated in Blender, along the correct Sun-Eros line.

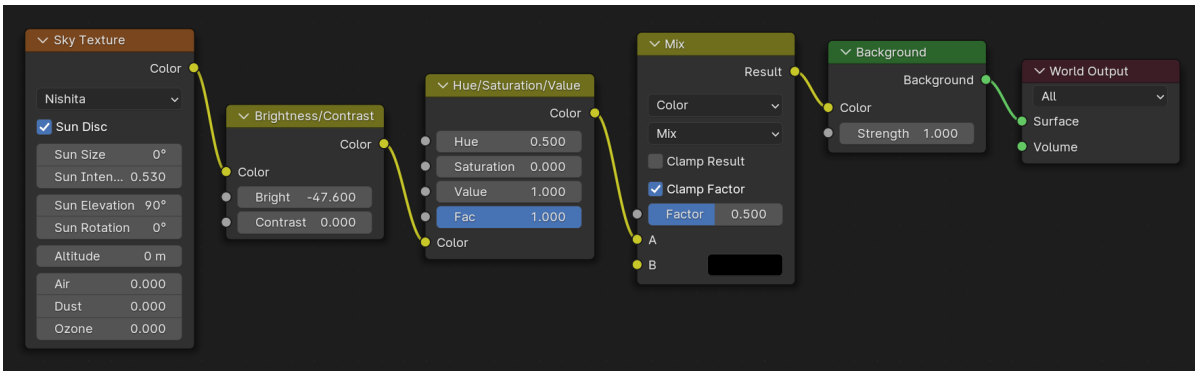

Figure B.1: Shading settings in Blender. With these settings the light as it would be in space is imitated.

Figure B.2 Shows the settings used for the “camera” when creating the rendered images in Blender. These settings are similar to the camera used in the experiment. No numerical faults were added, since the NUM datasets are used to find possible errors in the EXP datasets by comparing the two.

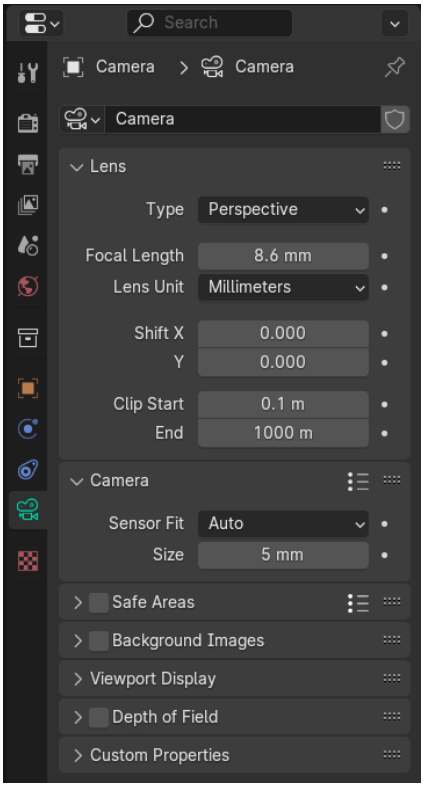

Figure B.2: Camera settings in Blender.

C

Calibration Measurements

Table C.1: CAL1_R_30

Image Size	[1080	1440]	[px]
Radial Distortion	[-0.0766	-0.068]	[-]
Tangential Distortion	[0	0]	[-]
Estimate Skew	0		[-]
Numerical Radial Distortion Coefficients	2		[-]
Estimate Tangential Distortion	0		[-]
Focal length	[2.4973E+03	2.4935E+03]	[px]
	[8.6157E-03	8.6026E-03]	[m]
Principal Point	[738.1034	517.8444]	[px]
Skew	0		[px]
Skew Error	0		[px]
Focal Length Error	[3.4397	3.3361]	[px]
Principal Point Error	[1.9027	2.2657]	[px]
Radial Distortion Error	[0.0113	0.1851]	[-]
Tangential Distortion Error	[0	0]	[-]

The camera calibration with the *MATLAB Single Camera Calibrator App* was completed for two orbits, 30 km and 200 km, and the two lighting scenarios. The outputs of these calibrations are given in the tables below. The image size is a given based on the sensor used by the camera. The other parameters are estimated in the calibration. The estimated distortions in the images are close to zero. The most important estimated parameters are the focal length and the principal point, since these parameters are directly used in the position estimate of the camera in the later analysis of the dataset.

Table C.2: CAL2_R_30

Image Size	[1080	1440]	[px]
Radial Distortion	[-0.0918	0.0173]	[-]
Tangential Distortion	[0	0]	[-]
Estimate Skew	0		[-]
Numerical Radial Distortion Coefficients	2		[-]
Estimate Tangential Distortion	0		[-]
Focal length	[2.4834E+03	2.4787E+03]	[px]
	[8.5677E-03	8.5515E-03]	[m]
Principal Point	[744.2581	518.5988]	[px]
Skew	0		[px]
Skew Error	0		[px]
Focal Length Error	[2.5546	2.4491]	[px]
Principal Point Error	[1.6434	1.878]	[px]
Radial Distortion Error	[0.0095	0.1461]	[-]
Tangential Distortion Error	[0	0]	[-]

Table C.3: CAL1_R_200

Image Size	[1080	1440]	[px]
Radial Distortion	[-0.1304	0.251]	[-]
Tangential Distortion	[0	0]	[-]
Estimate Skew	0		[-]
Numerical Radial Distortion Coefficients	2		[-]
Estimate Tangential Distortion	0		[-]
Focal length	[2.4595E+03	2.4603E+03]	[px]
	[8.4853E-03	8.4880E-03]	[m]
Principal Point	[736.2434	519.387]	[px]
Skew	0		[px]
Skew Error	0		[px]
Focal Length Error	[9.8164	9.8345]	[px]
Principal Point Error	[6.7461	7.02]	[px]
Radial Distortion Error	[0.01	0.0698]	[-]
Tangential Distortion Error	[0	0]	[-]

Table C.4: CAL2_R_200

Image Size	[1080	1440]	[px]
Radial Distortion	[-0.1163	0.1786]	[-]
Tangential Distortion	[0	0]	[-]
Estimate Skew	0		[-]
Numerical Radial Distortion Coefficients	2		[-]
Estimate Tangential Distortion	0		[-]
Focal length	[2.4957E+03	2.4958E+03]	[px]
	[8.6102E-03	8.6105E-03]	[m]
Principal Point	[746.9966	514.1391]	[px]
Skew	0		[px]
Skew Error	0		[px]
Focal Length Error	[13.4251	13.2823]	[px]
Principal Point Error	[6.453	6.8996]	[px]
Radial Distortion Error	[0.0122	0.1166]	[-]
Tangential Distortion Error	[0	0]	[-]

D

Result Addenda

D.1. Landmark points used in camera estimation

To estimate the camera position, the true locations of the landmarks used in the estimation have to be known. These locations were determined with Blender. The shape model was loaded into Blender at scale 1:1·10^3 and the landmark locations were determined by selecting the chosen landmarks and noting their position in the inertial reference frame of Blender. Table D.1 shows the landmarks used in the camera position estimation by location, per landmark, and per considered orbit and index. The landmarks used for orbits 100 km and 200 km are the same. The 30 km orbit used different landmarks, since only part of the asteroid is visible in each image and smaller landmarks can be identified.

Table D.1: Landmark positions on the surface of 433 Eros used in the camera estimation, in the inertial reference frame. There are N points for each image and each image is labelled with their respective index in the dataset.

p_N	x_N [km]	y_N [km]	z_N [km]	Orbit [km]	Index
1	-5.6863	-5.047	2.0038	30	1
2	-5.5545	-5.1226	1.7328	30	1
3	-1.0499	-4.7281	0.78017	30	1
4	-1.2967	-4.2567	2.9392	30	1
5	-3.0137	-3.8798	2.7348	30	1
6	-0.86489	-4.551	1.6983	30	1
7	-1.2846	-4.9645	-0.48693	30	1
8	0.51329	-5.0597	3.3131	30	1
1	-1.4467	-5.5751	0.65673	30	71
2	1.4415	-10.514	2.0604	30	71
3	0.047852	-8.2272	1.0605	30	71
4	0.67683	-8.9467	1.7542	30	71
5	2.6002	-12.86	1.0026	30	71
6	-3.6916	-1.1101	2.3086	30	71
7	-4.6808	-1.3696	0.00945	30	71
8	-4.352	-0.07364	2.5298	30	71
1	-2.6181	-11.661	1.29	30	121
2	2.106	-3.9402	1.1202	30	121
3	1.5554	-4.9277	-0.12016	30	121
4	-0.70038	-6.8477	2.3878	30	121
5	-1.0752	-7.768	2.454	30	121
6	0.38832	-6.4669	0.11389	30	121
7	2.8925	-3.1564	-1.0086	30	121
8	0.82471	-4.2924	2.4796	30	121
9	3.0864	-0.798	1.7386	30	121
10	-1.9536	-8.9137	2.6453	30	121
1	-5.6863	-5.047	2.0038	100	1
2	-5.5545	-5.1226	1.7328	100	1
3	-1.0499	-4.7281	0.78017	100	1

4	-14.896	2.2358	0.35693	100	1
5	5.7453	-2.5281	5.5642	100	1
6	-4.7113	-0.74775	5.717	100	1
7	-10.132	-1.8971	3.2148	100	1
8	13.825	-3.452	1.9162	100	1
9	10.616	-4.4231	2.2896	100	1
1	-10.38	11.923	1.9935	100	61
2	-7.5382	8.4904	3.4762	100	61
3	-4.3259	4.5013	3.961	100	61
4	-3.8655	0.21197	2.2657	100	61
5	-3.3488	-4.8856	0.32809	100	61
6	0.14077	-14.151	3.3728	100	61
7	2.1811	-9.9576	5.8546	100	61
8	1.7041	-15.607	1.5536	100	61
9	4.5776	-14.087	1.2457	100	61
10	9.0141	-6.9225	1.2729	100	61
1	-8.5506	-4.9167	0.52852	100	131
2	-3.2703	-14.701	3.5894	100	131
3	-1.585	-16.734	2.4782	100	131
4	0.20323	-11.825	3.501	100	131
5	2.5501	-0.25488	3.9715	100	131
6	4.6203	8.5838	5.859	100	131
7	3.7341	0.90508	2.1193	100	131
8	3.3625	-2.8544	0.615152	100	131
9	7.7912	6.6824	3.082	100	131
1	-5.6863	-5.047	2.0038	200	1
2	-5.5545	-5.1226	1.7328	200	1
3	-1.0499	-4.7281	0.78017	200	1
4	-9.1103	1.125	5.6643	200	1
5	-14.896	2.2358	0.35693	200	1
6	-1.2967	-4.2567	2.9392	200	1
7	17.422	0.45684	0.37107	200	1
8	11.934	-3.3615	2.9279	200	1
9	4.5803	-5.4531	3.4272	200	1
1	-10.38	11.923	1.9935	200	61
2	-7.5382	8.4904	3.4762	200	61
3	-4.3259	4.5013	3.961	200	61
4	-3.8655	0.21197	2.2657	200	61
5	-3.3488	-4.8856	0.32809	200	61
6	0.14077	-14.151	3.3728	200	61
7	2.1811	-9.9576	5.8546	200	61
8	1.7041	-15.607	1.5536	200	61
9	4.5776	-14.087	1.2457	200	61
10	9.0141	-6.9225	1.2729	200	61
1	-8.5506	-4.9167	0.52852	200	131
2	-3.2703	-14.701	3.5894	200	131
3	-1.585	-16.734	2.4782	200	131
4	0.20323	-11.825	3.501	200	131
5	2.5501	-0.25488	3.9715	200	131
6	4.6203	8.5838	5.859	200	131
7	3.7341	0.90508	2.1193	200	131
8	3.3625	-2.8544	0.615152	200	131
9	7.7912	6.6824	3.082	200	131

D.2. Imaging examples

Figure D.1 shows examples of the EXP images for each orbit and an example of the NUM images. The landmarks specified in Section D.1, are indicated in the images.

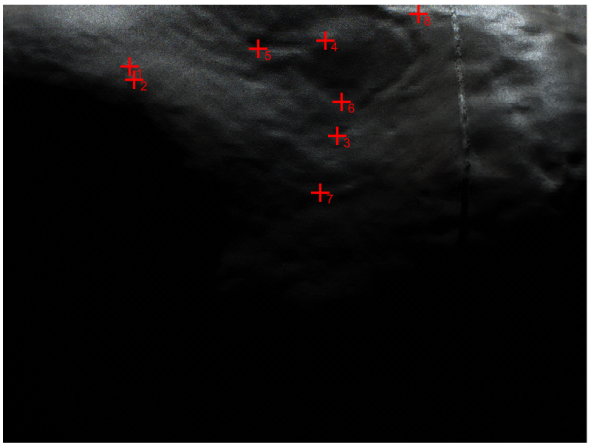

(a) EXP2_R_30_1

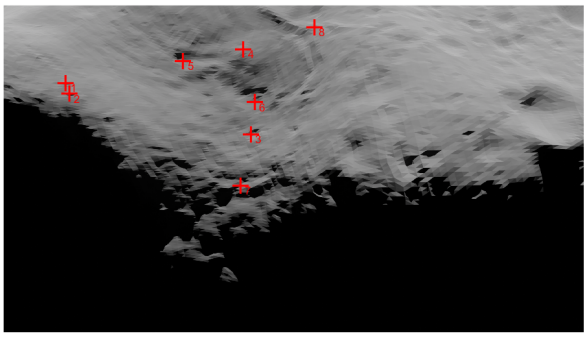

(b) NUM1_R_30_1

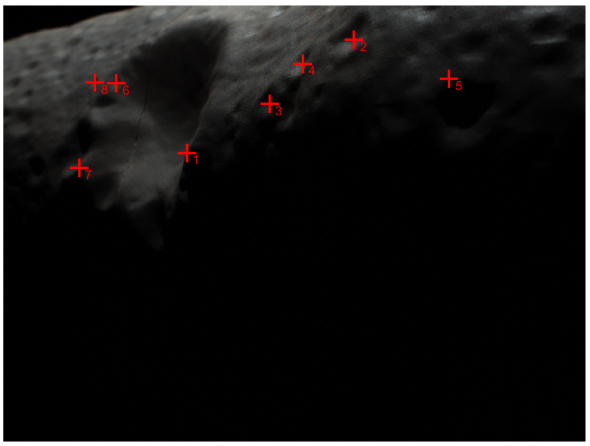

(c) EXP2_R_30_71

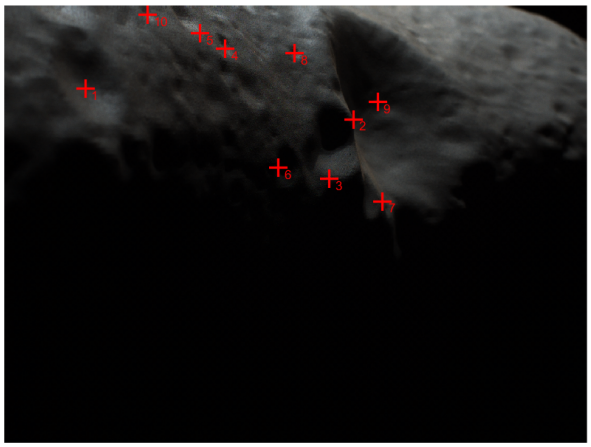

(d) EXP2_R_30_121

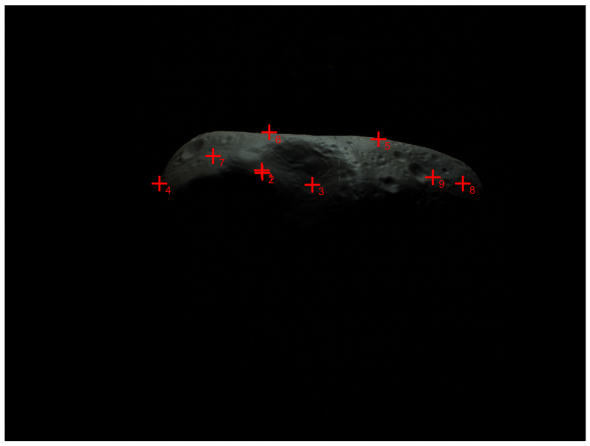

(e) EXP2_R_100_1

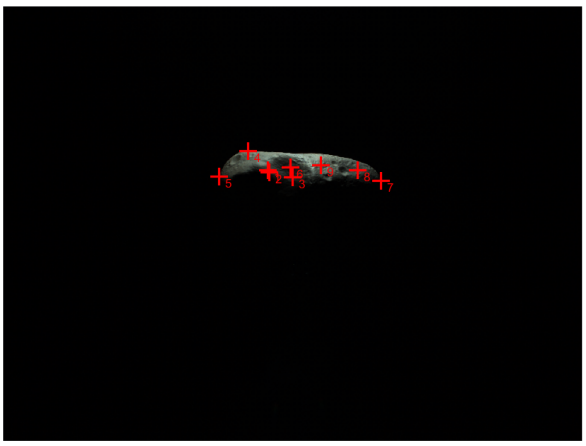

(f) EXP2_R_200_1

Figure D.1: Samples from the datasets with the landmarks used in the camera position estimation marked in the image.

D.3. Bias

Table D.2 shows the effect of the bias correction on the final camera position estimate. Both by the magnitude of the change in the Cartesian coordinate of the position estimate and the percent change between the original estimate and the estimate after the bias correction was applied.

Table D.2: Relative effect of bias correction on the Cartesian components of the camera position estimate and its error. First given in direct change in estimate, then in percent change between the magnitude of the new and old estimates.

Case	Δx [m]	Δy [m]	Δz [m]	Δe [m]	Δx [%]	Δy [%]	Δz [%]	Δe [%]	Orbit [km]	Index
EXP2	1599.33	63.09	1259.64	718.16	-85.5	0.23	-79.1	-19.2	30	1
	752.00	1023.83	1030.78	1135.13	-97.0	4.03	-65.7	-24.2	30	71
	974.32	1285.49	1335.28	794.82	-99.2	-4.59	-82.6	31.9	30	121
	1524.03	155.18	1916.44	622.14	-97.7	-0.16	-95.2	-15.2	100	1
	917.59	1006.25	1922.76	1433.80	-98.8	1.05	-93.4	-28.9	100	61
	831.11	732.00	1821.07	290.78	-96.6	-0.76	-92.9	6.7	100	131
	757.63	47.64	6435.29	3987.09	-99.8	0.02	-99.5	-55.1	200	1
	2889.97	3491.69	5937.44	5318.78	-99.1	1.84	-98.2	-42.7	200	61
	2992.83	2462.63	5806.73	482.82	-98.6	-1.29	-97.1	4.3	200	131
Average					**-96.9**	**0.04**	**-89.3**	**-15.8**		
NUM1	32.65	1.57	108.54	48.88	-66.8	0.01	-93.4	-35.3	30	1
	56.22	89.88	28.17	93.30	-88.2	0.30	-11.4	-25.7	30	71
	10.01	27.87	63.64	36.60	-97.8	-0.09	-69.4	-8.3	30	121
	114.26	15.94	373.72	316.43	-99.0	0.02	-98.9	-78.9	100	1
	111.98	137.40	360.39	261.04	-98.1	0.14	-98.0	-42.5	100	61
	72.56	76.08	318.57	38.70	-95.3	-0.08	-94.2	-8.1	100	131
	252.08	11.56	716.54	167.17	-99.1	0.01	-97.4	-9.1	200	1
	248.17	328.09	713.23	460.81	-97.1	0.17	-97.0	-22.1	200	61
	220.07	188.36	610.14	151.99	-91.2	-0.10	-86.6	3.2	200	131
Average					**-92.5**	**0.04**	**-82.9**	**-25.2**		